

Experimental Validation of a Coupled Fluid-Multibody Dynamics Model for Tanker Trucks

Tamer M. Wasfy

Advanced Science and Automation Corp.
Indianapolis, IN

James O'Kins; Scott Smith

U.S. Army Tank Automotive Research Development and
Engineering Center, Warren, MI

Copyright © 2008 SAE International

ABSTRACT

A time-accurate finite element model for predicting the coupled dynamic response of tanker trucks and their liquid payloads is presented along with an experimental validation of the model. The tanker truck components are modeled using rigid bodies, flexible bodies, joints and actuators. The model is validated using a full-scale army heavy class tactical trailer carrying a water tank. The trailer is placed on an n-post motion base simulator which was used to perform harmonic/ramp pitch, roll and stir excitations of the trailer in order to simulate typical road maneuvers. Experiments were carried out with an empty tank and a 65%-filled tank. The time-histories of the tires and suspension system deflections are measured for the various input motion excitations. The experiment's measurements are compared with the results predicted using the computational model. The comparison shows that the model can predict with reasonably good accuracy the test tanker-trailer's dynamic response.

1. INTRODUCTION

A time-accurate finite element model for predicting the coupled dynamic response of tanker trucks and their liquid payloads is presented along with an experimental validation of the model. Tanker trucks are used to transport liquids (such as fuels and water) from production facilities to distribution outlets. They provide the most flexible and readily deployable form of liquid transportation. Tanker trucks usually consist of a truck that may be pulling one or more trailers with one or more tanks carried on the truck and/or the trailer(s). Figure 1 shows a typical military tanker truck system consisting of a truck pulling a trailer that is carrying a potable water tank.

Many tanker truck accidents occur due to sloshing of the liquid payload when the tank is nearly half-full. The sloshing can shift the center of mass of the tank and can cause high time-varying inertia forces. This can cause the tanker truck to overturn, lose traction on one or more

tires, or be hard to brake or steer. All this can result in tanker-truck accidents which are costly and dangerous especially if the tank contains hazardous liquids (such as fuels, petrochemicals, or toxic liquids.) The estimated yearly cost of truck accidents in the US is about \$1.2 billion for trucks carrying hazardous material and \$43 billion for trucks carrying non-hazardous material [1]. The majority of those accidents (more than 75%) occur en-route. Accidents involving fire trucks account for approximately 20% of U.S. fire fighter deaths each year. Crashes involving fire trucks are the most prevalent of these types of accidents with 87% occurring when the fire truck went out of control and rolled over or left the road (no collision) [2]. The cost of physically building and testing tanker trucks can be very high. Several configurations with various shapes and locations for the baffles within the tanks, different tank geometries, and suspension system characteristics need to be tested. Considerable savings and better performance can be achieved if most of the testing is done numerically. The model presented and validated in this paper can help increase the stability, safety margins, maximum allowable speed, and/or liquid carrying capacity of tanker trucks and can help to reduce the annual costs of tanker truck accidents. It can also be used to investigate the cause of tanker truck accidents and to come up with the most effective design improvements that can increase the safety of tanker trucks.

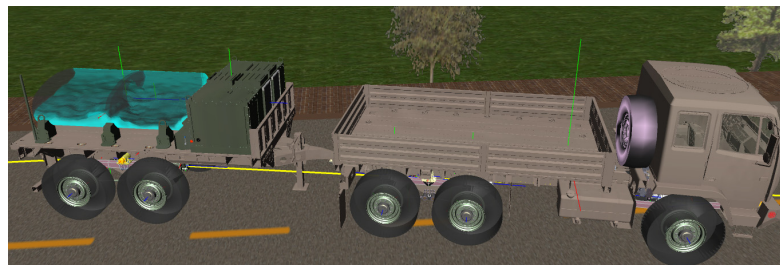


Figure 1 An FMTV (Family of Medium Tactical Vehicles) military tanker truck system consisting of a truck pulling a trailer that is carrying a water tank.

The model can also be easily extended to other applications involving flexible multibody systems carrying liquid filled tanks such as: tanker railroad cars, tanker ships, passenger cars (fuel-tanks), airplanes

Report Documentation Page			Form Approved OMB No. 0704-0188		
Public reporting burden for the collection of information is estimated to average 1 hour per response, including the time for reviewing instructions, searching existing data sources, gathering and maintaining the data needed, and completing and reviewing the collection of information. Send comments regarding this burden estimate or any other aspect of this collection of information, including suggestions for reducing this burden, to Washington Headquarters Services, Directorate for Information Operations and Reports, 1215 Jefferson Davis Highway, Suite 1204, Arlington VA 22202-4302. Respondents should be aware that notwithstanding any other provision of law, no person shall be subject to a penalty for failing to comply with a collection of information if it does not display a currently valid OMB control number.					
1. REPORT DATE 08 NOV 2007		2. REPORT TYPE N/A		3. DATES COVERED -	
4. TITLE AND SUBTITLE Experimental Validation of a Coupled Fluid-Multibody Dynamics Model for Tanker Trucks				5a. CONTRACT NUMBER	
				5b. GRANT NUMBER	
				5c. PROGRAM ELEMENT NUMBER	
6. AUTHOR(S) Tamer M. Wasfy; James O’Kins; Scott Smith				5d. PROJECT NUMBER	
				5e. TASK NUMBER	
				5f. WORK UNIT NUMBER	
7. PERFORMING ORGANIZATION NAME(S) AND ADDRESS(ES) US Army RDECOM-TARDEC 6501 E 11 Mile Rd Warren, MI 48397-5000				8. PERFORMING ORGANIZATION REPORT NUMBER 18435	
9. SPONSORING/MONITORING AGENCY NAME(S) AND ADDRESS(ES)				10. SPONSOR/MONITOR’S ACRONYM(S) TACOM/TARDEC	
				11. SPONSOR/MONITOR’S REPORT NUMBER(S) 18435	
12. DISTRIBUTION/AVAILABILITY STATEMENT Approved for public release, distribution unlimited					
13. SUPPLEMENTARY NOTES Presented at SAE World Congress, April 14-17, 2008, Detroit, MI, USA, The original document contains color images.					
14. ABSTRACT					
15. SUBJECT TERMS					
16. SECURITY CLASSIFICATION OF:			17. LIMITATION OF ABSTRACT SAR	18. NUMBER OF PAGES 18	19a. NAME OF RESPONSIBLE PERSON
a. REPORT unclassified	b. ABSTRACT unclassified	c. THIS PAGE unclassified			

(fuel-tanks and payload tanks), space launch vehicles (liquid fuel tanks), and satellites/space structures (liquid fuel tanks).

The experimental validation of the numerical model was carried out using a full-scale PLS (Palletized Load System) tanker-trailer that was instrumented and mounted on an n-post motion simulator (Figure 2). The n-post motion simulator consists of hydraulic linear actuators under each tire that can be independently controlled to simulate typical road maneuvers that the vehicle will be subjected to such as lane-change and going over symmetric or asymmetric bumps/potholes. Experiments were carried out with an empty tank and a 65% filled tank. The time-histories of the tires and suspension system deflections are measured for various input motion excitations. The measurements are compared with the results predicted using the computational model.



Figure 2 Instrumented PLS (Palletized Load System) tanker-trailer mounted on an n-post motion simulator that was used to validate the present finite element model.

In order to accurately predict the dynamic response of tanker trucks, the model must accurately account for the following effects:

- Incompressible liquid flow in a moving/deforming container (governed by the incompressible Navier-Stokes equations).
- Modeling of the liquid's free-surface.
- Modeling of fluid viscosity and turbulence.
- Coupling between the solid and the fluid at the fluid-structure interface.
- Large rotation of the solid bodies.
- Deformation of the solid flexible bodies. Flexible bodies can be modeled as springs, beam, shells or general solids. For example a general solid model can be used for leaf-springs while a linear-spring

model can be used to model struts and suspension springs.

- Joint kinematic constraints for spherical, revolute, cylindrical and prismatic joints including joint friction and clearances.
- Tire load-deflection and damping characteristics.
- Frictional contact between the tire and the terrain.
- Actuators and control laws.
- Motion control components including transmission components, clutches, and brakes (All those components involve friction).

In the present model, the fluid governing equations of motion are the incompressible Arbitrary Lagrangian-Eulerian Navier-Stokes equations along with a large-eddy simulation (LES) turbulence model. Incompressible fluid flow can be modeled using finite volume, finite element or particle methods. In addition, a technique for modeling the free-liquid surface must also be used. A literature review of the techniques for modeling fluid flow with a free-surface was presented in [3]. Those techniques are:

- Volume-of-fluid (VOF) method* [4-9]. Each element has a VOF value between 0 (for empty elements) and 1 (for elements completely filled with fluid). The free surface is reconstructed for each element using piecewise-linear planar segments that are calculated from the VOF value of the element along with the VOF values of neighboring elements (which are used to determine the normal to the planar surface).
- Level-set method*. This method uses a smooth scalar function defined at every node in the fluid domain which specifies the signed smallest Euclidian distance between the node and the interface [10]. The evolution of the scalar function is governed by a convection transport equation where the interface is moved with the fluid velocity.
- Arbitrary Lagrangian-Eulerian (ALE) method*. Using this method, the fluid mesh deforms and moves along with the fluid's free-surface [11-16]. A disadvantage of this method is that it does not allow large surface deformation including surface break-up and merging unless the fluid domain is re-meshed [14, 15].
- Lagrangian particle methods*. Lagrangian particles which represent small packets of fluid are used to model the fluid flow. A contact model between the fluid particles is used to model the fluid compressibility and viscous effects. A special type of this class of methods which has been successfully applied to free-surface flows and fluid-structure interaction problems is the particle finite element method (PFEM) [17] in which the particles are used to generate a polyhedral finite element mesh every time step using an extended Delaunay tessellation. The solution of the incompressible Navier-Stokes equations is then carried out using that mesh.

Techniques to handle fluid flow in a moving/deforming container were also reviewed in [3]. They include:

1. *Fixed Cartesian fluid mesh with cut-cell boundary condition.* The fluid domain is a Cartesian mesh [4, 5]. The container moves inside this mesh. A cut-cell technique is used to find where the boundary of the container intersects with the fluid cells.
2. *Moving ALE mesh.* The fluid is modeled using a fluid mesh that moves and deforms with the tank [3, 9, 11-13].
3. *Fixed-fluid mesh with the Navier-Stokes equations written in a reference frame fixed to the tank* [11, 18].
4. *Particle methods* [17]. Normal contact constraint between the particles and the tank wall is used to model the wall impenetrability constraint. Tangential friction between the particles and the tank wall is used to model wall adhesion and viscous effects.

In order to model fluid flow with a free-surface in a moving deforming container, the above methods must be combined. Table 1 shows the references where the various combinations of the above techniques were used.

Table 1 References for the various combinations of techniques for modeling a free-surface flow in a moving deforming container.

Free surface model	Moving / deforming tank model	Fixed grid	ALE	NS written in tank frame	Particles
VOF		4, 5	3, 9 (2D) Present paper	18	
Level-set			10		
ALE			11, 12, 13, 14, 15, 16	11	
Particles					17

In the present paper, an acceptor-donor VOF based algorithm is used to model the free-surface and the ALE method is used for modeling fluid flow in a moving/deforming container. Using the VOF technique for modeling the free-surface has the following advantages over other methods:

- The VOF technique can conserve mass and energy better than the level-set method. This is due to the fact that the VOF technique explicitly balances local mass transfers between elements. On the other hand, the level-set method relies on the fluid flow solution to conserve mass and uses interpolated velocities which can lead to accumulation of mass loss or gain errors.
- Unlike the ALE technique, the VOF technique can handle fluid breakup and merging without the need for re-meshing. If re-meshing is used frequently, it can degrade the solution accuracy due to re-interpolation of the solution field onto the new mesh.
- Particle methods require a large number of particles to accurately model the free surface. The PFEM requires less fluid particles, however, the tessellation step is computationally intensive.

Using the ALE method for modeling the moving/deforming container has the following advantages over other methods:

- In the fixed Cartesian fluid mesh method, since the solid container cuts the mesh cells at arbitrary surfaces, the fluid-solid impenetrability and no-slip boundary conditions are satisfied only in a time average sense. Also, the method has stability and accuracy problems when the cut-cell elements at the solid-fluid interface become small. In addition, for tanker truck applications, since the tank can undergo very large translation as the truck is moving on the road, the Cartesian mesh must be moved with the tank. This means the fluid mesh is no longer fixed, and that an ALE formulation must be used to move the mesh. This reduces the simplicity of the method.
- The main disadvantage of using a fixed-fluid mesh with the Navier-Stokes equations written in a reference frame fixed to the tank is that since the tank frame is a non-inertial frame (accelerating frame), writing the equations of motion with respect to that frame results in a complex inertia operator which involves centrifugal and Coriolis acceleration terms. Also, this method cannot - by itself - deal with a deforming container.

A review of multibody dynamics modeling techniques including deformation reference frames, treatment of large rotations, discretization techniques, finite elements, constraint and contact modeling, and solution techniques is presented in [19]. In the present paper, a flexible multibody dynamics code with the following characteristics is used:

- The solid, fluid and fluid-solid interface governing equations of motion are solved along with joint/constraint equations using a time-accurate explicit solution procedure that can maintain time-accuracy over long simulation times. The explicit solution procedure was presented in Ref. [3] and, for the sake of completeness, is outlined in the Appendix.
- Total Lagrangian, total displacement equations of motion formulation with the degrees of freedom referred to a global inertial reference frame [15-18].
- Flexible bodies can be modeled using a library of spring, truss, beam, and solid nonlinear finite elements with Cartesian coordinate degrees of freedom. This allows arbitrarily large element rotations. The elements library includes:
 - Struts and suspension springs, that are modeled using a linear spring element, that can include a prescribed stiffness-deflection relation, a damping-deflection rate relation and a friction coefficient-deflection rate relation.
 - Torsional-spring type 3-node beam elements [20, 21].
 - Natural-modes eight-node brick elements [22, 23]. Those elements can also be used

to model shells and beams. One element through the thickness is sufficient to accurately model the membrane, shear, and bending characteristics. They do not exhibit locking or spurious modes (widely used techniques to alleviate locking such as hourglass control lead to elements that do not maintain solution accuracy over very long solution times). They are computationally efficient. Assumed strain elements of comparable accuracy are more computationally expensive. Any material law can be used with those elements including: linear elastic, hyper-elastic, and non-linear laws. Leaf-springs are modeled using the natural-modes brick elements.

- Connection points on the rigid and flexible bodies are used to define joints between the bodies including spherical, revolute, cylindrical, prismatic and rigid joints. A penalty model is used to impose the joint/contact constraints [24]. An asperity-based friction model is used to model joint/contact friction [25].
- Rigid body rotational equations of motion are written in a body (material) frame, with the resulting incremental rotations added to the total body rotation matrix [24]. The rigid bodies rotational equations of motion are written in a body-fixed frame with the total rigid-body rotation matrix updated each time step using incremental rotations.
- Normal contact is modeled using a penalty formulation [26, 27]. Frictional contact is modeled using an accurate and efficient asperity-based friction model [25]. Tires are modeled using a one node tire model that accounts for distributed tire normal contact using the penalty formulation and friction using the asperity-based friction model.
- Special elements are used to model wheels/pulleys [26, 27], sprockets [28], and clutches [29].
- The code uses a general contact search algorithm that finds the contact penetration between finite elements and other elements as well as general triangle and quadrilateral surfaces.

Two-way coupling between the multibody system (vehicle) motion and the fluid is achieved by satisfying the following conditions at the solid-fluid interface:

- The fluid velocity normal to the solid's surface must be equal to the normal solid velocity.
- The fluid velocity tangent to the solid surface can range from being equal to the tangential velocity of the solid surface (no slip condition) to being free.
- No additional energy or momentum to the system should be introduced at the interface.

The above boundary conditions are satisfied by solving Newton's equations of motion at the fluid-solid interface nodes for a common normal acceleration for the fluid

and the solid at the interface. The tangential fluid and solid accelerations can range from being the same (no-slip condition) to being completely decoupled.

In the present paper, a single computational code which uses a time-accurate explicit solution procedure is used to solve both the solid and fluid equations of motion. Many commercial software and studies on modeling liquid sloshing coupled with solid body motion use two codes which pass the interface forces and motion back and forth and iterate on the two codes until equilibrium is achieved [e.g. 6, 18]. This approach adds extra computational burden and, in general, does not achieve the same accuracy as the single integrated code solution due to the difficulty in achieving an equilibrium solution between two disjointed codes.

The rest of this paper is organized as follows. In Section 2 the equations of motion for the solid, fluid and fluid-structure interface are presented. In Section 3 the frictional contact model is presented along with a description of the 1-node distributed contact tire model. In Section 4 the VOF free-surface model is presented. In Section 5 the experimental setup along with the validation study are presented. Finally, in Section 6 concluding remarks are offered.

2. EQUATIONS OF MOTION

In the subsequent equations the following conventions will be used:

- The indicial notation is used.
- The Einstein summation convention is used for repeated subscript indices unless otherwise noted.
- Upper case subscript indices denote node numbers.
- Lower case subscript indices denote vector component number.
- The superscript denotes time.
- A superposed dot denotes a time derivative.

2.1 SOLID EQUATIONS OF MOTION

The solid translational equations of motion are written with respect to the global inertial reference frame and are obtained by assembling the element equations. The finite elements used here use only translational DOFs with no rotational DOFs. The translational equations of motion include the rigid-body translational DOFs. They can be written as:

$$M_K \ddot{x}_{Ki}^t = F_{sKi}^t + F_{aKi}^t \quad (1)$$

where t is the running time, K is the global node number (no summation over K ; $K=1 \rightarrow N$ where N is the total number of nodes), i is the coordinate number ($i=1,2,3$), a superposed dot indicates a time derivative, M_K is the lumped mass of node K , x is the vector of nodal Cartesian coordinates with respect to the global inertial reference frame, and \ddot{x} is the vector of nodal accelerations with respect to the global inertial reference frame, F_s is the vector of internal structural forces, and F_a is the vector of externally applied forces, which include surface forces and body forces.

For each rigid body, a body-fixed material frame is defined. The rigid body is represented by one node located at the body's center of mass, which is also the origin of this frame. The mass of the body is concentrated at the node and the inertia of the body, given by the inertia tensor I_{ij} , is defined with respect to the body frame. The orientation of the body-frame is given by R_K^t which is the rotation matrix relative to the global inertial frame at time t_0 . The rotational equations of motions are written for each rigid body with respect to its body-fixed material frames as:

$$I_{Kij} \ddot{\theta}_{Kj}^t = T_{sKi}^t + T_{aKi}^t - (\dot{\theta}_{Ki}^t \times (I_{Kij} \dot{\theta}_{Kj}^t))_{Ki} \quad (2)$$

where I_K is the inertia tensor of rigid body K , $\ddot{\theta}_{Kj}$ and $\dot{\theta}_{Kj}$ are the angular acceleration and velocity vectors' components for rigid body K relative to its material frame in direction j , T_{sKi}^t is the component of the vector of internal torque at node K in direction i , and T_{aKi}^t is the component of the vector of applied torque in direction i . The summation convention is used only for the lower case indices i and j .

The trapezoidal rule is used as the time integration formula for solving equation (1) for the global nodal positions x :

$$\dot{x}_{Kj}^t = \dot{x}_{Kj}^{t-\Delta t} + 0.5 \Delta t (\ddot{x}_{Kj}^t + \ddot{x}_{Kj}^{t-\Delta t}) \quad (3a)$$

$$x_{Kj}^t = x_{Kj}^{t-\Delta t} + 0.5 \Delta t (\dot{x}_{Kj}^t + \dot{x}_{Kj}^{t-\Delta t}) \quad (3b)$$

where Δt is the time step. The trapezoidal rule is also used as the time integration formula for the nodal rotation increments:

$$\dot{\theta}_{Kj}^t = \dot{\theta}_{Kj}^{t-\Delta t} + 0.5 \Delta t (\ddot{\theta}_{Kj}^t + \ddot{\theta}_{Kj}^{t-\Delta t}) \quad (4a)$$

$$\Delta \theta_{Kj}^t = 0.5 \Delta t (\dot{\theta}_{Kj}^t + \dot{\theta}_{Kj}^{t-\Delta t}) \quad (4b)$$

where $\Delta \theta_{Kj}$ are the incremental rotation angles around the three body axes for body K . The rotation matrix of body K (R_K) is then evaluated using:

$$R_K^t = R_K^{t-\Delta t} R(\Delta \theta_{Kj}^t) \quad (5)$$

where $R(\Delta \theta_{Kj}^t)$ is the rotation matrix corresponding to the incremental rotation angles from Equation (4b).

The explicit solution procedure used for solving equations (1-5) along with the constraint equations is presented in Section 6. The constraint equations are generally algebraic equations, which describe the position or velocity of some of the nodes. They include:

- Prescribed motion constraints:

$$f(\{x\}, t) = 0 \quad (6)$$

- Joint constraints:

$$f(\{x\}) = 0 \quad (7)$$

- Contact/impact constraints:

$$f(\{x\}) \geq 0 \quad (8)$$

The penalty technique is used for imposing the constraints in which a normal reaction force is generated when a node penetrates into a contact body. The magnitude of the force is proportional to the penetration distance [24-26].

2.2 FLUID EQUATIONS OF MOTION

The dynamic response of the fluid is described by the ALE version of the incompressible Navier-Stokes equations. Namely, the equations of conservation of momentum and mass for a moving deforming control volume along with a large-eddy simulation (LES) transport equation. Those are:

$$\int_V \rho \frac{\partial u_i}{\partial t} dV = \int_V -u_i \frac{\partial \rho}{\partial t} dV + \int_V \frac{\partial [-\rho u_i \hat{u}_j - P \delta_{ij} + \tau_{ij}]}{\partial x_j} dV + \int_V \rho f_i dV \quad (9)$$

$$\int_V \frac{\partial \rho}{\partial t} dV + \int_V \frac{\partial (\rho \hat{u}_i)}{\partial x_i} dV = 0 \quad (10)$$

$$\rho = \rho_0 + r P \quad (11)$$

$$\hat{u}_i = u_i - v_i \quad (12)$$

$$\tau_{ij} = \lambda D_{kk} \delta_{ij} + 2(\mu + \mu_t) D_{ij} \quad (13a)$$

$$D_{ij} = 0.5(\hat{u}_i / \partial x_j + \hat{u}_j / \partial x_i) \quad (13b)$$

$$\int_V \frac{\partial (\rho K)}{\partial t} dV = - \int_V \frac{\partial (\rho \hat{u}_i K)}{\partial x_i} dV + \int_V \frac{\partial}{\partial x_i} \left[(\mu + \mu_t) \frac{\partial K}{\partial x_i} \right] dV + \int_V \left(2\mu_t D_{ij} - \frac{2}{3} \rho K \partial_{ij} \right) \frac{\partial \hat{u}_i}{\partial x_j} dV - \int_V \rho \varepsilon dV \quad (14)$$

$$\varepsilon = 1.0 K^{3/2} \quad (15a)$$

$$\mu_t = 0.05 \sqrt{K} \quad (15b)$$

where V is the element volume, t is the running time, ρ is the density of the fluid, \vec{u} is the fluid velocity vector relative to the global reference frame, $\vec{\hat{u}}$ is the fluid velocity vector relative to the moving fluid mesh, \vec{v} is the velocity of the fluid mesh, P is the relative pressure, \vec{x} is the position vector, τ is the deviatoric stress tensor, D is the rate of deformation tensor, \vec{f} is the body force vector, r is the artificial compressibility parameter, ρ_0 is the nominal fluid density, μ is the fluid viscosity, μ_t is an additional turbulence viscosity calculated using Equation 15b), K is the eddy kinetic energy, and ε is the sub-grid scale eddy kinetic energy dissipation term. Incompressible flow is modeled using the artificial compressibility technique [30]. A finite element formulation is used to derive the element's semi-discrete equations of motion from the governing equations (9-13). 8-node hexahedral elements are used with tri-linear equal-order velocity and pressure interpolation. A pressure averaging algorithm [31] is used to eliminate pressure checker-boarding (due to the use of an equal order interpolation for pressure and velocity). The element equations are assembled into the global semi-discrete equations of motion:

$$M_{fN} \dot{u}_{Ni}^t = F_{fNi}^t \quad (16)$$

$$V_{fN} \dot{P}_N^t = Q_{fN}^t \quad (17)$$

$$M_{fK} \dot{K}_N^t = S_{fN}^t \quad (18)$$

where M_{fN} is the lumped fluid mass of node N , \dot{u}_{Ni}^t is component i of the fluid acceleration at node N , F_{fNi}^t is component i of the fluid forces at node N , V_{fN} is the lumped fluid volume at node N , \dot{P}_N^t is the fluid pressure rate at node N , Q_{fN}^t is the fluid pressure flux at node N , \dot{K}_N^t is the eddy kinetic energy rate at node N , and S_{fN}^t is the eddy kinetic energy flux at node N . Those equations are integrated using the trapezoidal rule along with an

explicit solution procedure to yield the nodal fluid velocity and pressure:

$$u_{Kj}^t = u_{Kj}^{t-\Delta t} + 0.5 \Delta t (\dot{u}_{Kj}^t + \dot{u}_{Kj}^{t-\Delta t}) \quad (19)$$

$$P_{Kj}^t = P_{Kj}^{t-\Delta t} + 0.5 \Delta t (\dot{P}_{Kj}^t + \dot{P}_{Kj}^{t-\Delta t}) \quad (20)$$

$$K_{Kj}^t = K_{Kj}^{t-\Delta t} + 0.5 \Delta t (\dot{K}_{Kj}^t + \dot{K}_{Kj}^{t-\Delta t}) \quad (21)$$

2.3 FLUID-STRUCTURE INTERFACE EQUATIONS OF MOTION

Newton's equations of motion are used to find a common normal acceleration for the fluid and the solid at the interface. This is done for each node at the fluid-structure boundary as follows:

$$(m_s + m_f) \ddot{u}_n = \sum \text{FluidForces} + \sum \text{StructureForces} \quad (22a)$$

$$(m_s + m_f) \ddot{v}_n = \sum \text{FluidForces} + \sum \text{StructureForces} \quad (22b)$$

where m_s is the solid mass of the node, m_f is the fluid mass of the node, \ddot{u}_n and \ddot{v}_n are respectively the fluid and solid accelerations of the node normal to the fluid-structure interface. The tangential fluid and solid accelerations (\ddot{u}_t, \ddot{v}_t) are calculated using the following equations:

$$((1-s)m_s + m_f) \ddot{u}_t = (1-s) \sum \text{StructureForces} + \sum \text{FluidForces} \quad (23a)$$

$$(m_s + (1-s)m_f) \ddot{v}_t = \sum \text{StructureForces} + (1-s) \sum \text{FluidForces} \quad (23b)$$

where s is the slip factor. A no-slip condition corresponds to a slip factor of zero. The slip factor determines how much of the fluid and structure forces are mutually exchanged. Equations 22 and 23 are written for all fluid-solid interface nodes. The fluid mesh must move and deform with the tank. This is done by modeling the fluid mesh using very light and compliant (3 orders of magnitude less than the tank) solid brick elements (called "mock" mesh). The ALE formulation is used to account for the fluid mesh deformation/motion.

3. TIRE FRICTIONAL CONTACT MODEL

A tire is mounted on a rigid body representing the wheel. Contact is detected between the tire's surface and a polygonal surface representing the contact body. The tire's external surface is discretized in the circumference and meridian directions into a grid of rectangles with a contact point defined at the center of each rectangle (Figure 3). The global position (x_{Gcp}) and velocity (\dot{x}_{Gcp}) of a contact point is obtained using the rigid body position and rotation matrix:

$$x_{Gcp_i} = X_{BF_i} + R_{BF_{ij}} x_{Lcp_j} \quad (24)$$

$$\dot{x}_{Gcp_i} = \dot{X}_{BF_i} + R_{BF_{ij}} (W_{BF} \times x_{Lcp})_j \quad (25)$$

where X_{BF} and \dot{X}_{BF} are the global position and velocity vectors of the wheel's frame, R_{BF} is the rotation matrix of the wheel relative to the global reference frame, W_{BF} is the wheel's angular velocity vector relative the local wheel's frame, and x_{Lcp} is the position of the contact point relative to the wheel's frame. The frictional contact force at each contact point (sum of the normal contact and tangential friction forces) is transferred as a force and a moment to the center of the wheel. The negative of this force is transferred to the center of the contact

body. Those forces and moments are summed and applied as external forces to the wheel and contact body.

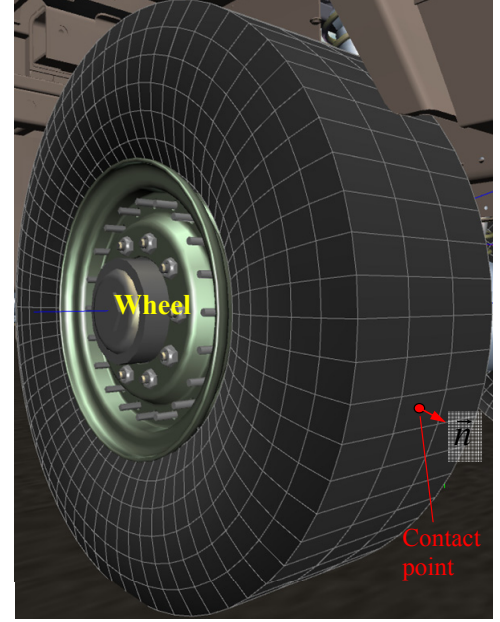


Figure 3 Tire mounted on a wheel and discretized into a grid of rectangular elements with a typical contact point at the center of an element.

3.1 PENALTY NORMAL CONTACT MODEL

The penalty technique is used for imposing the contact constraints. In this technique, a normal reaction force (F_{normal}) is generated when a contact point is in contact with a body (i.e. when the point is inside the body) that is given by [25, 26]:

$$F_{normal} = A k_p d + A \begin{cases} c_p \dot{d} & \dot{d} \geq 0 \\ s_p c_p \dot{d} & \dot{d} < 0 \end{cases} \quad (26)$$

where A is the area of the rectangle associated with the contact point, k_p and c_p are the penalty stiffness and damping coefficient per unit area; d is the closest distance between the node and the contact surface (Figure 4); s_p is a separation damping factor between 0 and 1 which determines the amount of sticking between the contact node and the contact surface at the node (leaving the body). The normal contact force vector is given by:

$$F_{n_i} = n_i F_{normal} \quad (27)$$

where \vec{n} is the normal to the surface. The total force on the node generated due to the frictional contact between the point and surface is given by:

$$F_{po \text{ int } i} = F_{t_i} + F_{n_i} \quad (28)$$

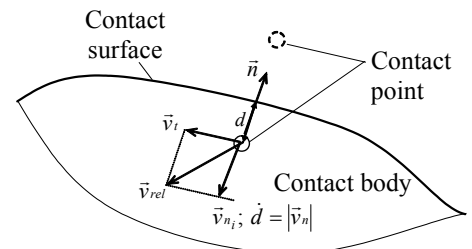


Figure 4 Contact surface and contact node.

3.2 ASPERITY FRICTION MODEL

The frictional contact force (given by the asperity friction model described below) transmitted to the contact body at the contact point is $-\vec{F}_{node} \cdot \vec{F}_{tj}$ is given by:

$$F_{tj} = F_{tangent} \quad t_j \quad (29)$$

An asperity friction model is used along with the normal force to calculate the tangential friction force ($F_{tangent}$) [25]. The basic idea of the model is that friction between two rough surfaces in contact arises due to the interaction of the surface asperities. When two surfaces are in static (stick) contact, the surface asperities act like tangential springs. When a tangential force is applied, the springs elastically deform and pull the surfaces to their original position. If the tangential force is large enough, the surface asperities yield (i.e. the springs break) allowing sliding to occur between the two surfaces. The breakaway force is proportional to the normal contact pressure. In addition, when the two surfaces are sliding past each other, the asperities provide resistance to the motion that is a function of the sliding velocity and acceleration, and the normal contact pressure. Figure 5 shows a schematic diagram of the asperity friction model. It is composed of a simple piece-wise linear velocity-dependent approximate Coulomb friction element (that only includes two linear segments) in parallel with a variable anchor point spring.

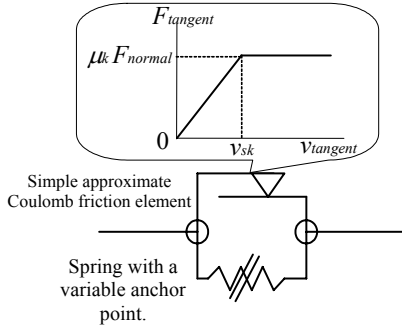


Figure 5 Asperity spring friction model.

3.3 CONTACT SEARCH

Contact between each contact point on the tire and the contact surface(s) (which are polygonal surfaces) is detected using a binary tree contact search algorithm which allows fast contact search. The algorithm works by recursively dividing the polygonal surface into 2 blocks of polygons and then finding the bounding box for each block of polygons. If the contact point is inside a bounding box then the two sub-bounding boxes are checked to determine if the point is inside either one. The recursion stops when the bounding box contains 3 polygons or less. At that point a more computationally intensive contact algorithm between a point and a polygon is used to determine the depth of contact.

4. VOF FREE-SURFACE MODEL

For each fluid element a VOF value between 0 and 1 is defined, where 0 corresponds to empty elements and 1 corresponds to elements completely filled with fluid. The

elements' VOF values are updated each time-step by moving fluid from a completely or partially filled “donor” element to an empty or partially filled neighboring “acceptor” element using the following model:

$$V_{eo} = V_e \text{ VOF}_e \quad (30)$$

$$V_{na} = V_n (1 - \text{VOF}_n) \quad (31)$$

$$\Delta V = \begin{cases} \Delta t S A \vec{n} \cdot \vec{u} & V_{eo} > \Delta V \text{ and } V_{na} > V_{eo} \\ V_{eo} & V_{eo} < \Delta V \\ V_{na} & V_{na} < \Delta V \end{cases} \quad (32)$$

where V_e is the volume of the element; V_n is the volume of the neighboring element; V_{eo} is the volume of the element occupied by the fluid; V_{na} is the volume of the neighboring element available to receive fluid; ΔV is the volume flow through the boundary between the two elements in a time step; Δt is the solution time step; S is the surface area between the two elements; A is a value between 0 and 1 indicating the free-surface aperture through which the fluid can move from the element to the neighboring element; \vec{n} is a unit vector normal to S ; and \vec{u} is the fluid velocity vector at the surface S . If ΔV is less than 0 then the element is an acceptor element and the VOF values are not updated because they will be updated later when the neighboring element is set to be the donor element. If ΔV is greater than 0 then the VOF values are updated using the following equations:

$$\text{VOF}_e = \text{VOF}_e - \Delta V / V_e \quad (33)$$

$$\text{VOF}_n = \text{VOF}_n + \Delta V / V_n \quad (34)$$

The free-surface apertures A at the element interfaces are used to limit the fluid flow based on the location of the free surface inside the element. A is calculated as follows. If the VOF value of the element is 1 then there is no free-surface at the element, therefore $A=1$. For elements with a VOF value less than 1, the following steps are used to calculate A :

- Calculate the normal to the surface by looking at a stencil of neighboring elements around the element. This is done using the following equation:

$$n_{e_i} = \text{VOF}_{n_k} S_{n_k} n_{n_{ki}} \quad i=1, 2, 3 \quad (35)$$

where n_{e_i} is the i^{th} component of the normal to the free-surface at the element, VOF_{n_k} is the VOF value for neighboring element number k , S_{n_k} is the area of the intersection surface between the element and neighboring element k , and $n_{n_{ki}}$ is the component i of the normal to the surface between the element and neighboring element k . \vec{n}_e is then normalized into a unit vector. Figure 6 shows a 2D 4-node quadrilateral and the free-surface along with the normal \vec{n}_e .

- Calculate the apertures A for each neighboring element by constructing a planar surface with normal \vec{n}_e and with total volume equal to $\text{VOF}_e V_e$ (see Figure 6).

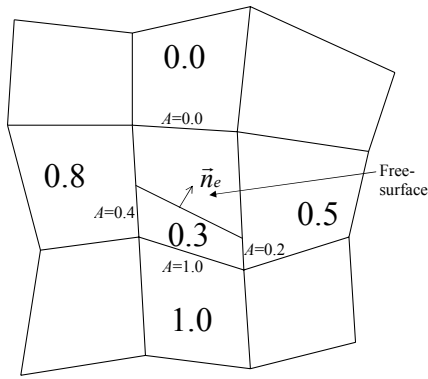


Figure 6 Stencil of neighboring elements used to determine the free-surface normal \vec{n}_e and the liquid free-surface.

5. VALIDATION STUDY

The model is validated using a full-scale army heavy class tactical PLS (Palletized-Load System) trailer carrying a potable water tank module (called Hippo). The trailer was placed on an n-post motion base simulator in TARDEC's Simulation Laboratory (TSL) (Figure 7). The n-post motion simulator consists of linear hydraulic actuators each placed under one of the trailer's tires. Each actuator has one degree of freedom along the vertical direction and can be independently commanded to follow a certain vertical displacement time-history. Thus, the actuators can be controlled in such a way as to simulate vertical position time-histories of the wheels during typical road maneuvers. These maneuvers can include: traversing a bumpy terrain, going over symmetric or asymmetric bumps, turning and lane-change. Note that the motion simulator cannot simulate the inertial centrifugal and Coriolis forces that arise due to the time-varying motion of the trailer on the road.



Figure 7 Experimental setup consisting of a PLS trailer carrying a "Hippo" tank module mounted on an n-post motion simulator and instrumented to measure the tire and suspension system deflection time-histories.

The trailer in our experimental setup has 3 axles. We call the axles: front axle, back axle 1 and back axle 2 (Figure 8). The trailer also has 6 wheels: front right, front left, back 1 right, back 1 left, back 2 right and back 2 left.

Each hydraulic actuator is composed of a cylinder, piston and a dishpan where the tire rests. The front and back axle 1 actuators had trapezoidal dishpans for

safety reasons. This is in order to ensure that the trailer does not slide off the motion simulator (Figure 9). The two back axle 2 actuators had flat dishpans. In addition, a wire harness was attached to the top of the trailer at all time during the experiments for safety reasons. The wire harness was loose so as not to interfere with the vibration results of the trailer.

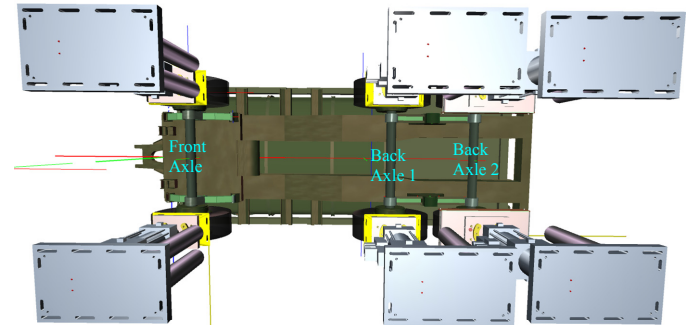


Figure 8 Bottom view of the trailer showing the three axles.

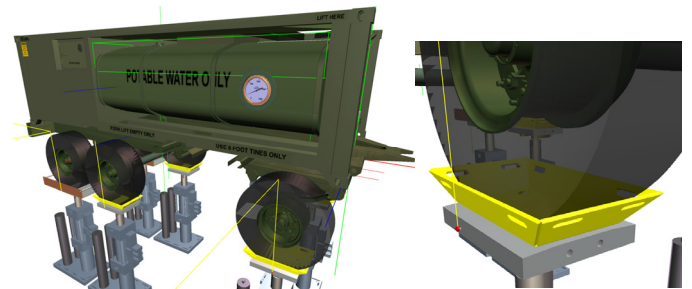


Figure 9 Side view of the trailer (left) showing the trapezoidal dishpans in yellow on the front axle tires and back axle 1 tires. Back axle 2 tires have flat dishpans.

Displacement data is measured using LVDTs. All LVDT signals are sampled at a rate of 256 samples/sec. Figure 10 shows a picture of the trailer along with the displacement data collected during the experiments. The experiment displacement measurements are compared with the results predicted using the computational model. Displacement is measured at 22 points. They are:

- Linear vertical input motion of the 6 actuators (labeled: Front left actuator; Front right actuator; Back 1 left actuator; Back 1 right actuator; Back 2 left actuator; Back 2 right actuator).
- Linear vertical motion of each wheel's center relative to the trailer's frame (labeled: Front left wheel; Front right wheel; Back 1 left wheel; Back 1 right wheel; Back 2 left wheel; Back 2 right wheel).
- Linear vertical deflection of each tire obtained by measuring the distance between the center of the wheel and the dishpan (labeled: Front left tire; Front right tire; Back 1 left tire; Back 1 right tire; Back 2 left tire; Back 2 right tire).
- Longitudinal displacements of the trailer's frame relative to ground measured on the Left and right of the trailer's frame (Labeled: Left long.; Right long.).
- Lateral displacements of the trailer's frame relative to ground measured near the front and back 2 axles (Labeled Front lateral; Back lateral).

A camera mounted on the ground is used to record the motion of the trailer tank. The camera is set to capture 30 frames/sec. The camera view is shown in Figure 7.

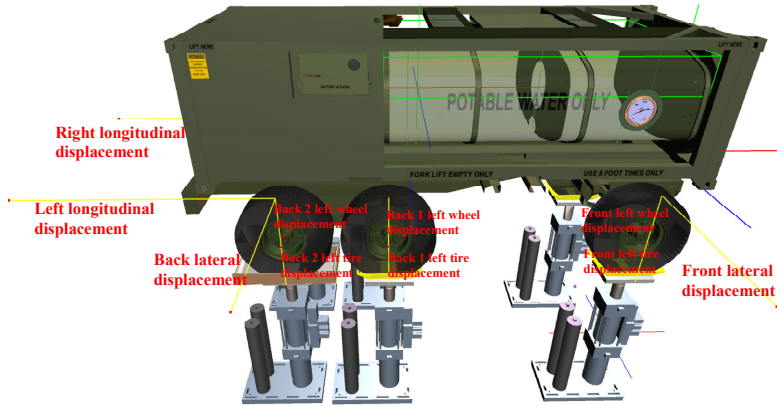


Figure 10 Displacement data collected during the experiments.

Table 2 Trailer empty tank experiments (26 experiments).

	Pitch		Roll		Stir	
	Freq. (Hz)	Amp. (mm)	Freq. (Hz)	Amp. (mm)	Freq. (Hz)	Amplitude (mm)
Harmonic excitation	0.7	100	0.5	36	0.5	50
	0.7	140	0.5	48	0.5	70
	1.0	60	1.0	20	0.6	50
	1.0	75	1.0	30	0.6	70
	1.5	20	1.5	5	1.0	30
	1.5	25	1.5	7	1.0	40
	2.0	17	2.0	28		
Ramp excitation	Amp. (mm)		Amplitude (mm)		Amplitude (mm)	
	63 (0.1 sec ramp)		45 (0.1 sec ramp)		155 (0.1sec ramp LF)	
	110(0.2sec ramp)		50 (0.2sec ramp)		110 (0.1sec ramp LB)	

Table 3 Trailer 65% filled-tank experiments (Total of 26 experiments).

	Pitch		Roll		Stir	
	Freq. (Hz)	Amp. (mm)	Freq. (Hz)	Amp. (mm)	Freq. (Hz)	Amp. (mm)
Harmonic excitation	0.7	100	0.5	36	0.5	50
	0.7	140	0.5	48	0.5	70
	1.0	60	1.0	20	0.6	50
	1.0	75	1.0	30	0.6	70
	1.5	20	1.5	8	1.0	30
	1.5	25	1.5	12	1.0	40
	2.0	17	2.0	30		
Ramp excitation	Amp. (mm)		Amp. (mm)		Amplitude (mm)	
	70 (0.1sec ramp)		50 (0.1 sec ramp)		180 (0.1sec ramp LF)	
	120 (0.2sec ramp)		55 (0.2 sec ramp)		110 (0.1sec ramp LB)	

Experiments were carried out with an empty tank and a 65%-filled tank. The time-histories of the displacements at the 22 points described above are collected for various input motion excitations. Those include pitch, roll and stir. Pitch excitation simulates both sides of the trailer going over a symmetric bump/pothole. Roll motion simulates the trailer turning or going over a bump/pothole only on one side of the trailer. The stir motion simulates a combination of pitch and roll motions. For each motion type either a harmonic excitation or a ramp excitation was used. For the harmonic excitation the frequency and amplitude of the excitation is varied. The harmonic excitation experiments are conducted by slowly ramping up the amplitude of the excitation to the full amplitude. For the ramp excitation just the amplitude of the excitation is varied. Table 2 shows the experiments carried out with the empty tank. Table 3 shows the experiments carried out with the tank 65%

filled with water. For the harmonic excitations the specified amplitude is the peak-to-peak amplitude. For the ramp excitations, the amplitude is the difference between the initial value and the final value after the ramp. The two actuators under the left two back tires are always moved the same way. Similarly, the two actuators under the right two back tires are always moved the same way. The experiments are performed as follows:

- In the pitch experiments the left and right actuators move in phase. The actuators for the two back axes are moved 180° out-of-phase with the front actuators.
- In the roll experiments left and right actuators move 180° out-of-phase. The two back axes and the front actuators move in-phase.
- In the harmonic stir experiments the front left, front right, back right, and back left actuators are 90° out-of-phase.
- In the ramp stir experiments either the left front (LF) or the two left back (LB) actuators are moved.

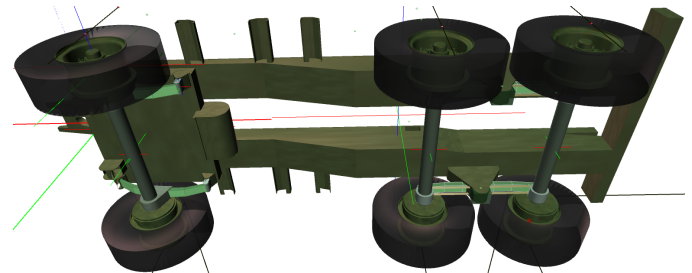


Figure 11 Trailer model.

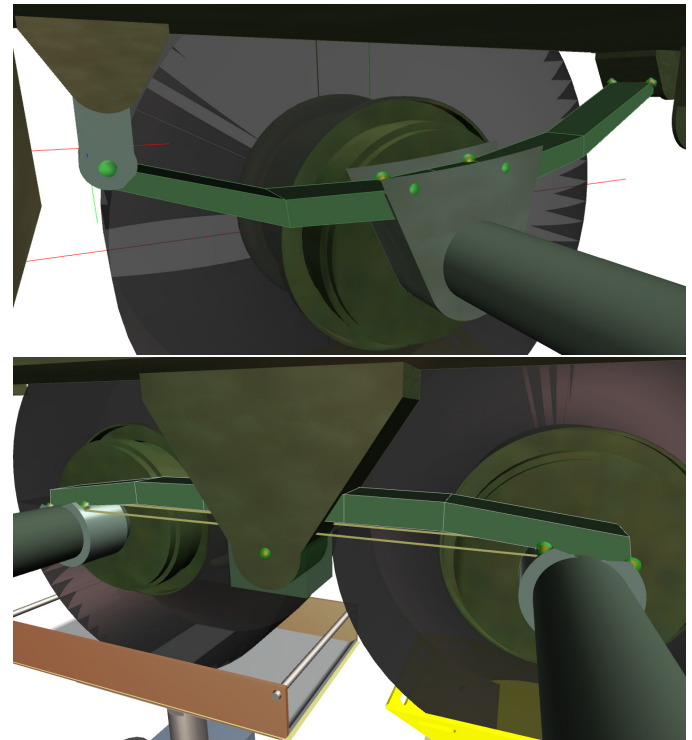


Figure 12 Front leaf-spring (top) back leaf-spring (bottom) modeled using brick elements. Connection points are shown as green spheres.

The modeling techniques presented in this paper were implemented in the DIS [32] commercial finite element code. The DIS code was used to numerically simulate

the experiments in Tables 2-3. The simulation results are then compared to the experiment results. A DIS finite element model of the trailer and the n-post motion simulator was constructed. The model has 33548 nodes and consists of the following components:

- *A rigid grounded base.*
- Rigid bodies representing the chassis, 3 axles, and suspension system elements (Figure 11).
- *6 linear actuators.* The actuator cylinders are part of the grounded base and the actuator pistons and dishpans are modeled as rigid bodies (Figure 10). Two parallel cylindrical joints are used at each actuator to model a prismatic joint that allows the actuator to move only along the vertical direction.
- 2 front and 2 back leaf-springs modeled using brick elements (Figure 12).
- 6 wheels modeled using rigid bodies. A tire is mounted on each wheel. The tire is in contact with the dishpan of the corresponding actuator piston (Figure 9).
- *An oval tank.* The tank is modeled as a rigid body. The tank is discretized using 33516 hexahedral fluid elements (Figure 13). The tank has a cross-section baffle near it's center. The baffle has a big round opening at the center and small openings near the bottom and top of the tank to equalize the liquid level.
- *Spherical joints* are used to model the suspension system connections and the wheels' connections to the axles.

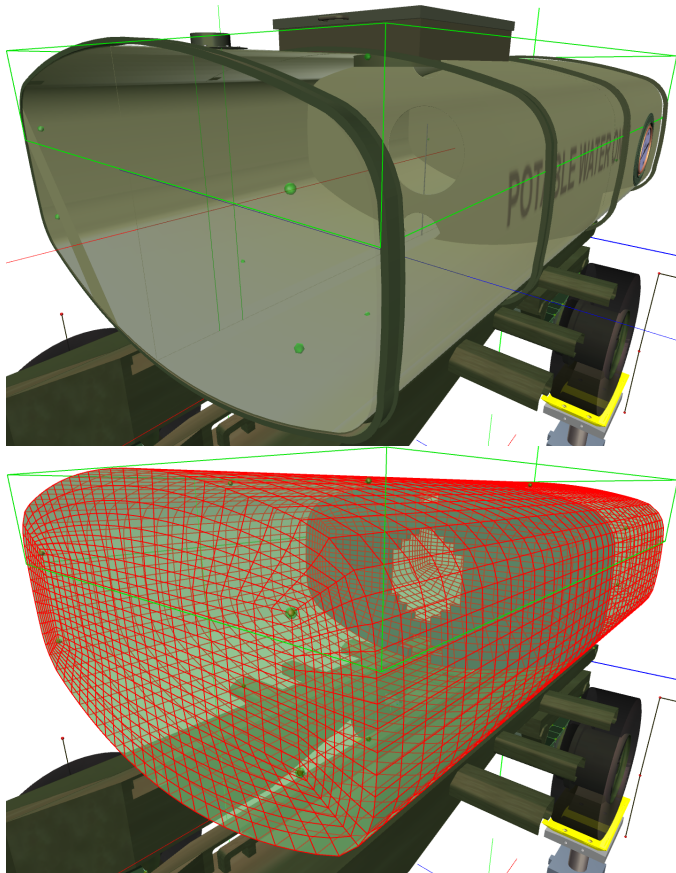


Figure 13 Tank geometric model (top) finite element model (bottom).

Water ($\rho = 1000 \text{ Kg/m}^3$, $\mu = 0.001 \text{ Kg/m.sec}$) is modeled as incompressible using the artificial compressibility technique with an artificial sound speed factor of 0.1 (i.e. the artificial sound speed in the water is taken as $1483 \text{ m/sec} \times 0.1 = 148.3 \text{ m/sec}$). Due to the use of large elements near the solid surface, full slip boundary condition at the wall is used ($s = 1$ in Equation 23). Thus, the viscous wall friction effects are assumed to be negligible. Gravity is modeled with the gravitational acceleration taken to be 9.8 m/sec^2 in the vertical direction. The explicit time step was $1.53 \times 10^{-5} \text{ sec}$.

After performing the simulations, we determined that the trapezoidal dishpans that were used for the front and back axle 1 tires in order to ensure that the trailer does not slide off the motion simulator, affected the displacement response at those dishpans. This is due to the fact that the sides of the tires were in contact with the sides of the trapezoidal dishpans. This produced friction forces which made the tire stick to the dishpan whenever the dishpan is trying to pull away from the tire. The 1-node tire model is not adequate for modeling this because it does not account for the tire deformation with respect to the wheel. This is due to the fact that the finite element node of the wheel is also used for the tire contact and deformation calculations. In order to account for the deformation of the tire with respect to the wheel a detailed finite element model of the tire is needed similar to the model developed in Ref. [27]. For practical applications, the side of the tire is not in contact with the terrain, therefore, the 1-node tire model can model with adequate accuracy the tire's response. The flat dishpans used for the back axle 2 tires do not have this problem and therefore the 1-node tire model is adequate. In the present paper, all the runs were performed using the 1-node tire model. Therefore we will present the results for the back axle 2. In a future paper, we will present the results with a detailed finite element tire model for the trailer's tires.

The graphs in Figures 14-29 show a comparison of the DIS simulation and experiment displacements at the back axle 2 of the trailer (back 2 left wheel; back 2 right wheel; back 2 left tire; back 2 right tire) for eight empty tank and eight 65%-filled tank experiments. The average difference in magnitude and frequency between the experiment and simulation is about 15-20% in the graphs shown in Figures 14-29. The average difference in magnitude and frequency between the experiment and simulation for the front and back axle 2 displacements was about 30% on average due to the presence of the trapezoidal dishpans as mentioned above. There was no significant difference in the magnitude of the experiment to simulation error between the empty tank runs and the 65%-filled tank runs. In the opinion of the authors, the main sources of error between the experiments and simulation in order of importance are:

- The trapezoidal dishpans at the front and back axle 1 tires, affected the back axle 2 response.

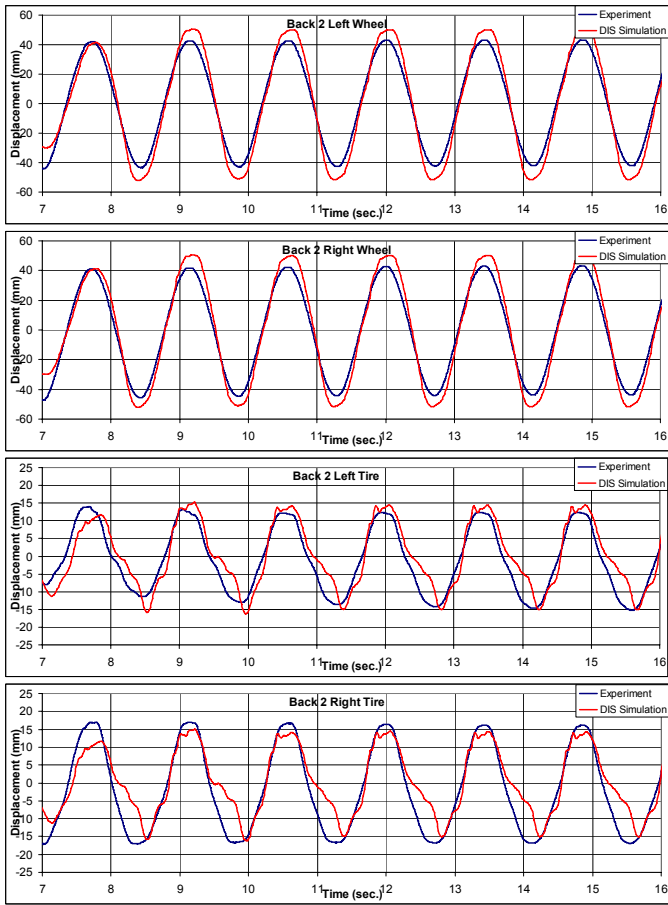


Figure 14 Comparison between the experiment and DIS simulation for an empty tank with a pitch 0.7 Hz, 140 mm harmonic excitation.

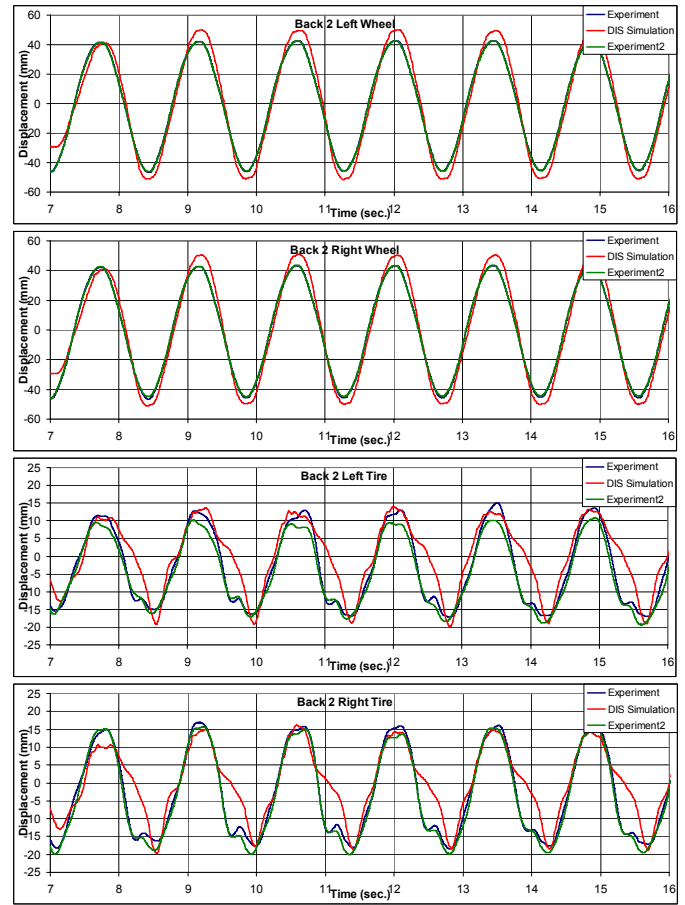


Figure 15 Comparison between the experiment and DIS simulation for a 65% filled tank with a pitch 0.7 Hz, 140 mm harmonic excitation.

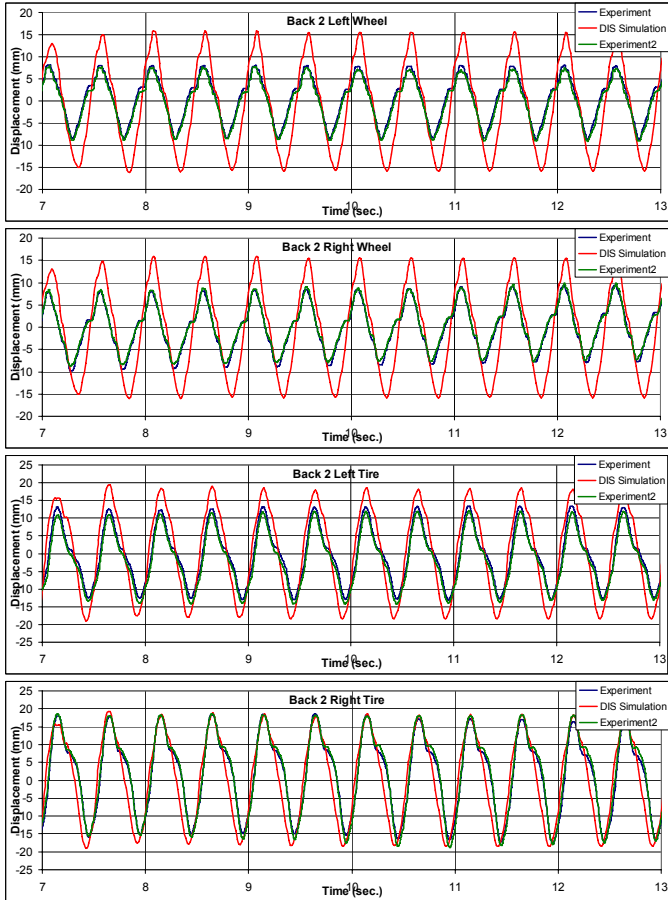


Figure 16 Comparison between the experiment and DIS simulation for an empty tank with a pitch 2.0 Hz, 17 mm harmonic excitation.

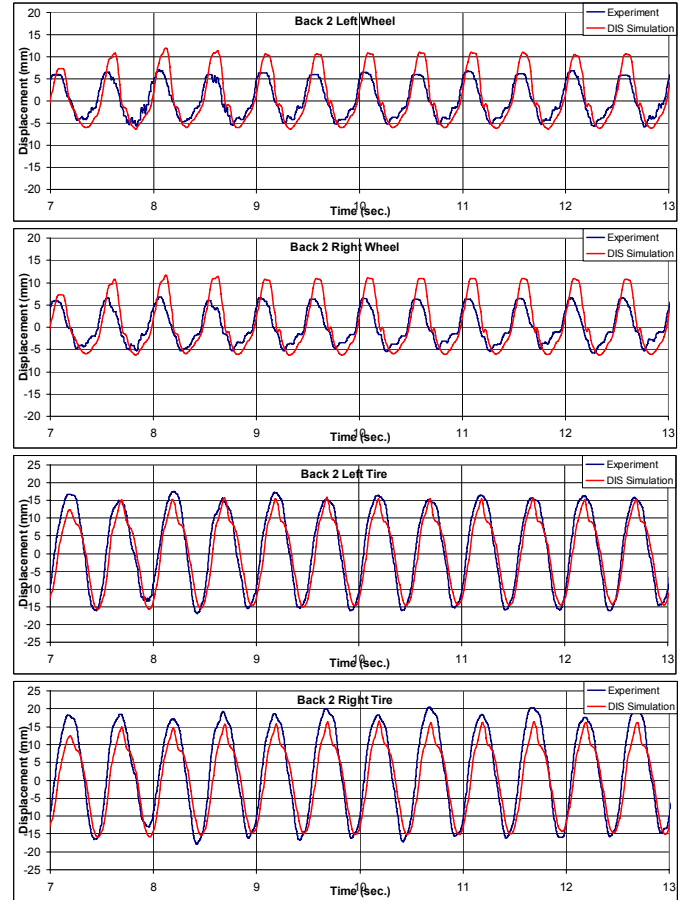


Figure 17 Comparison between the experiment and DIS simulation for a 65% filled tank with a pitch 2.0 Hz, 17 mm harmonic excitation.

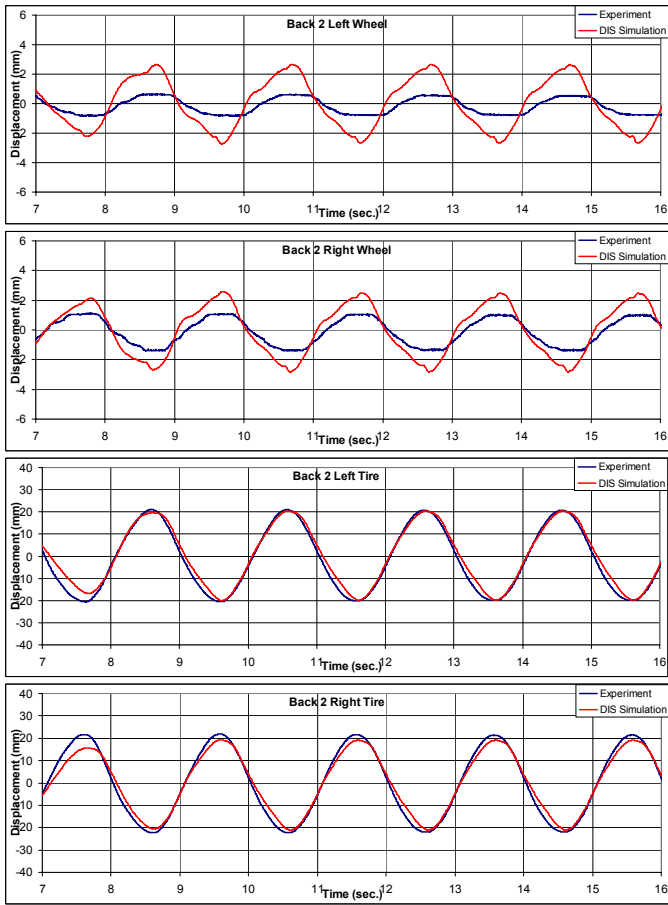


Figure 18 Comparison between the experiment and DIS simulation for an empty tank with a roll 0.5 Hz, 48 mm harmonic excitation.

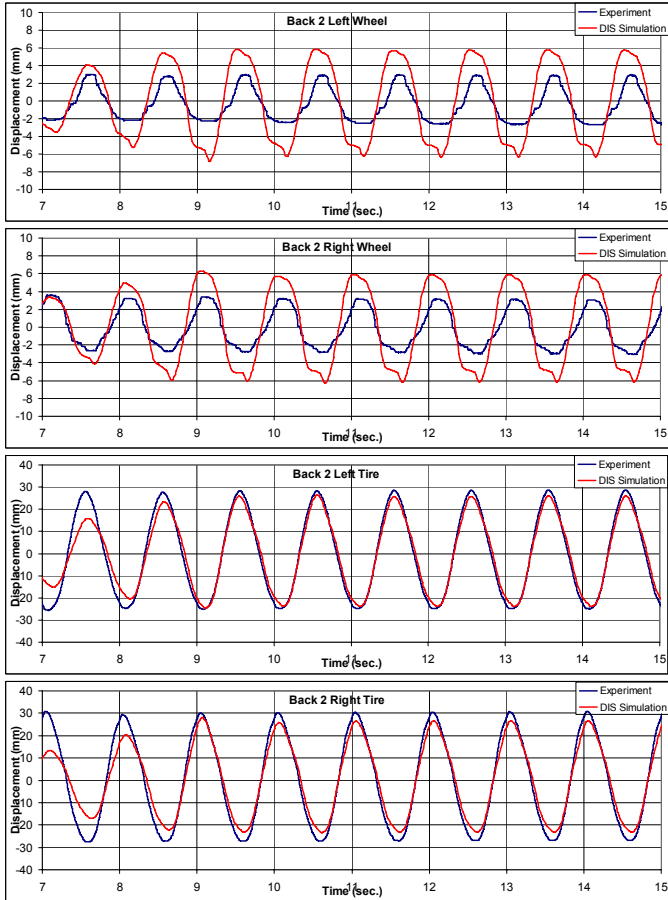


Figure 20 Comparison between the experiment and DIS simulation for an empty tank with a roll 1.0 Hz, 30 mm harmonic excitation.

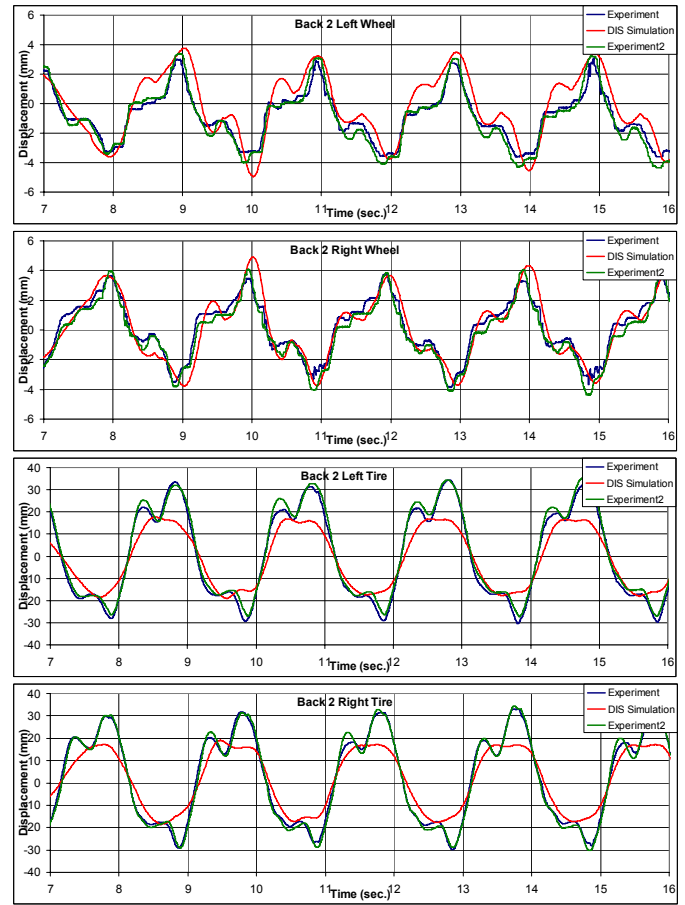


Figure 19 Comparison between the experiment and DIS simulation for a 65% filled tank with a roll 0.5 Hz, 48 mm harmonic excitation.

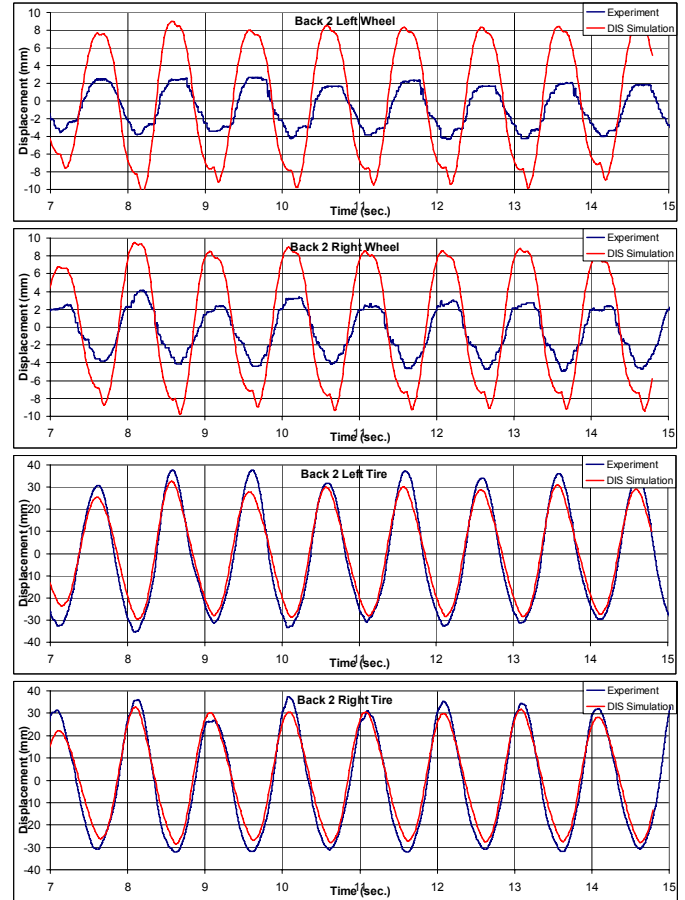


Figure 21 Comparison between the experiment and DIS simulation for a 65% filled tank with a roll 1.0 Hz, 30 mm harmonic excitation.

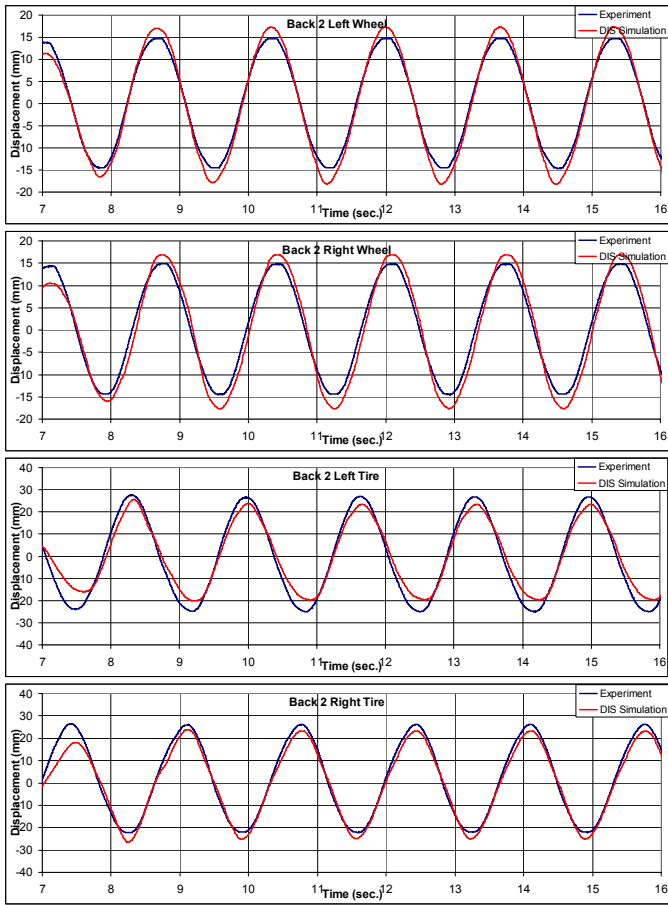


Figure 22 Comparison between the experiment and DIS simulation for an empty tank with a stir 0.6 Hz, 70 mm harmonic excitation.

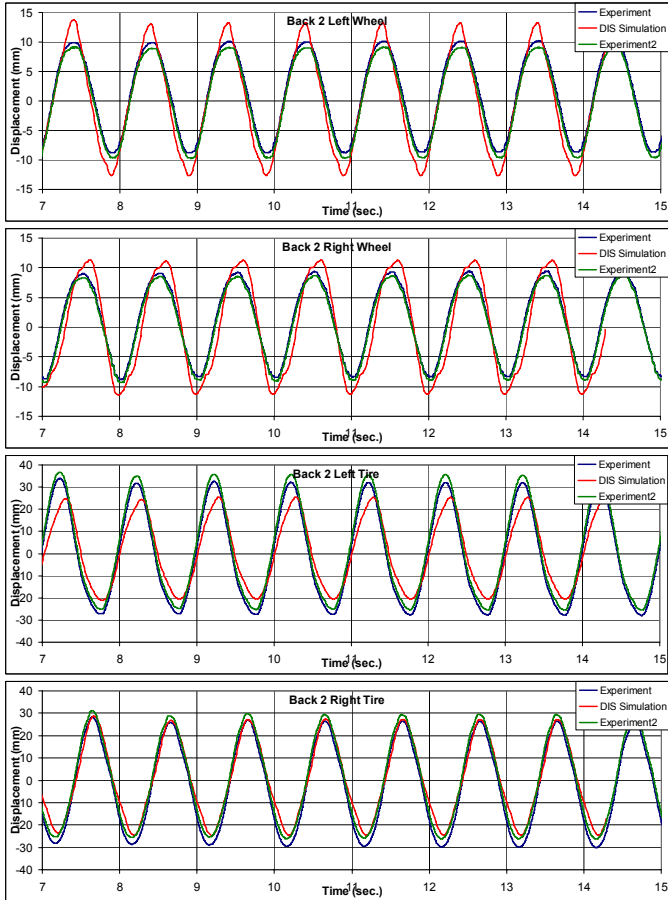


Figure 24 Comparison between the experiment and DIS simulation for an empty tank with a stir 1.0 Hz, 40 mm harmonic excitation.

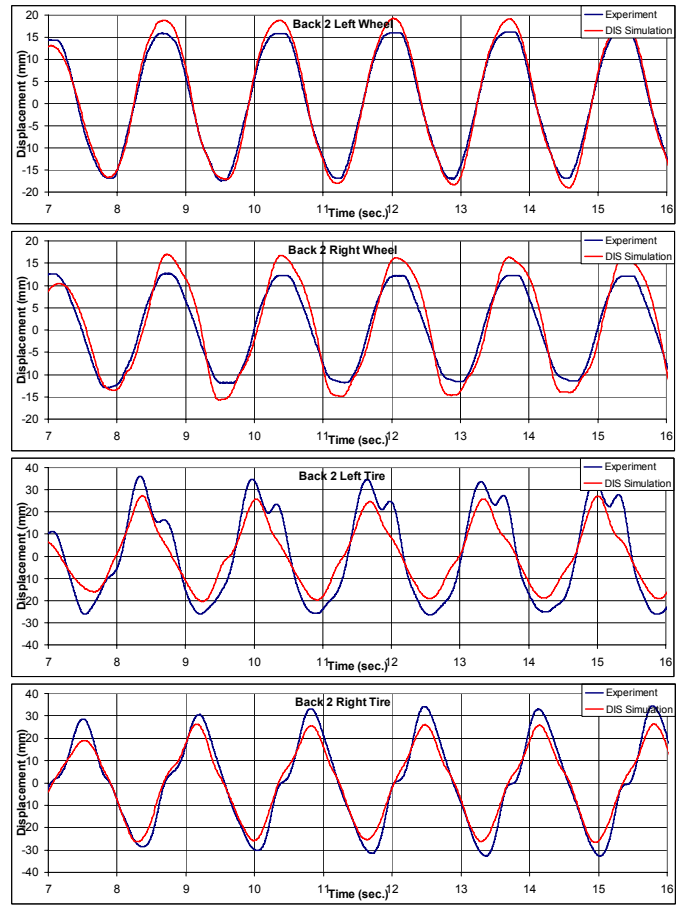


Figure 23 Comparison between the experiment and DIS simulation for a 65%-filled tank with a stir 0.6 Hz, 70 mm harmonic excitation.

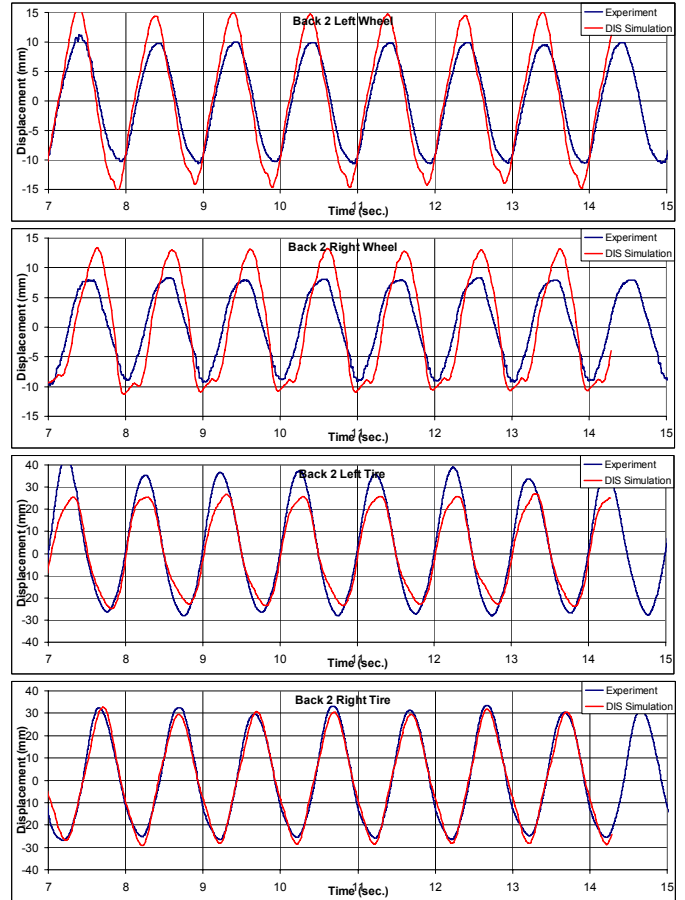


Figure 25 Comparison between the experiment and DIS simulation for a 65%-filled tank with a stir 1.0 Hz, 40 mm harmonic excitation.

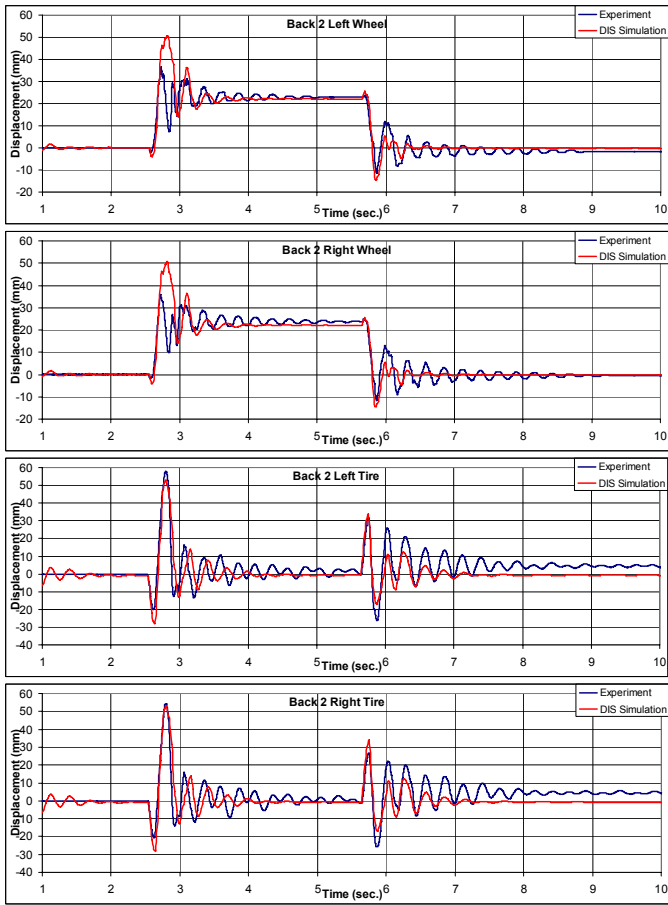


Figure 26 Comparison between the experiment and DIS simulation for an empty tank with a pitch 0.1 sec. 63 mm ramp excitation.

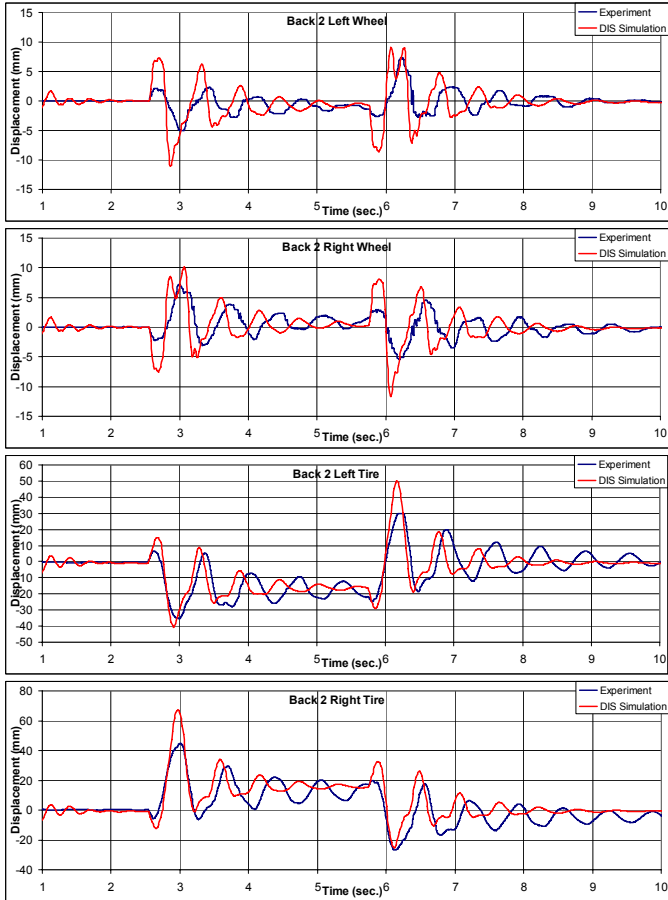


Figure 28 Comparison between the experiment and DIS simulation for an empty tank with a roll 0.2 sec. 50 mm ramp excitation.

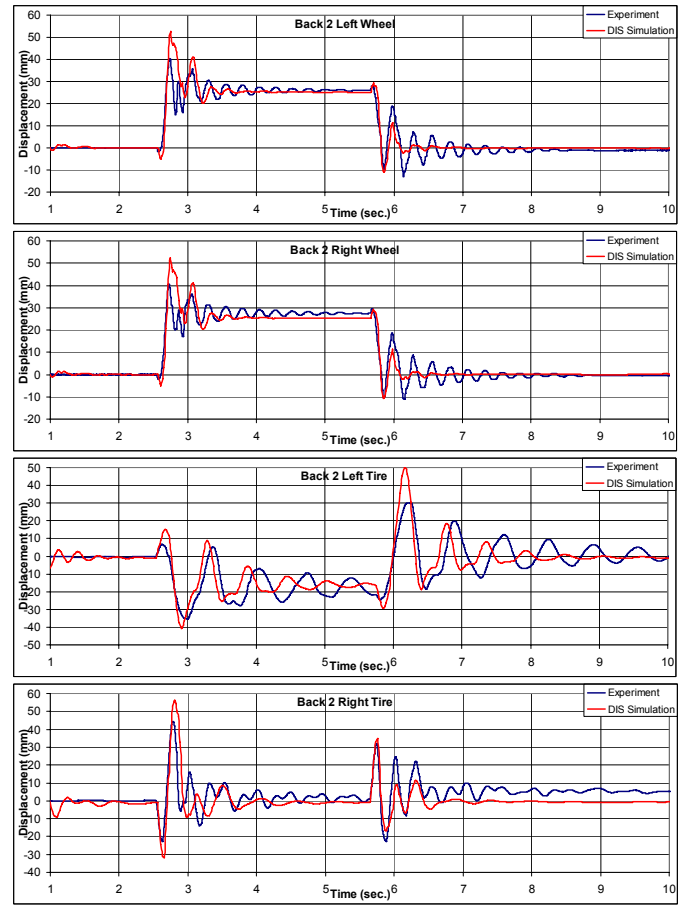


Figure 27 Comparison between the experiment and DIS simulation for a 65%-filled tank with a pitch 0.1 sec. 70 mm ramp excitation.

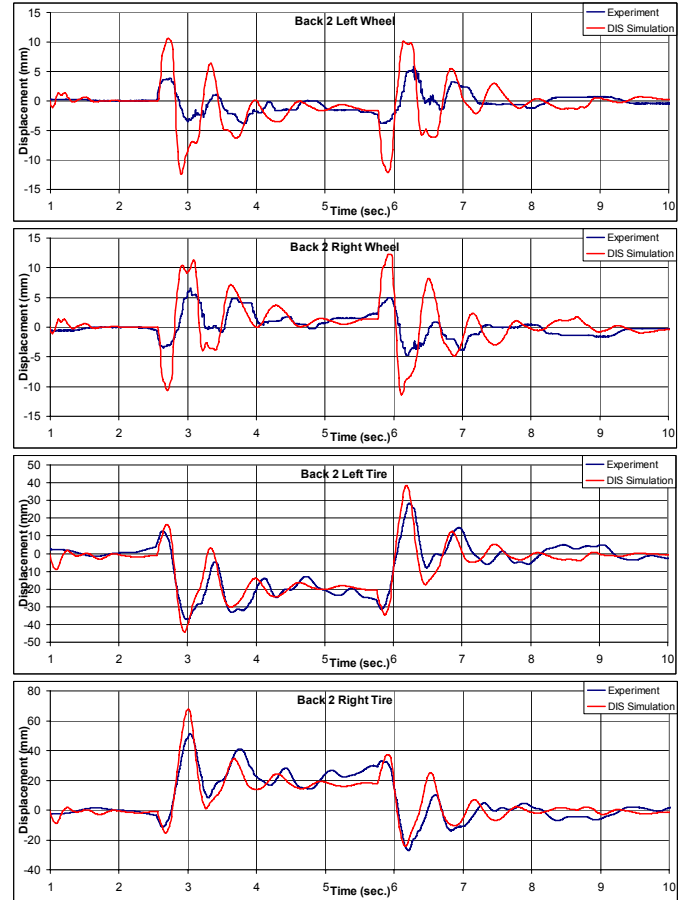


Figure 29 Comparison between the experiment and DIS simulation for a 65%-filled tank with a roll 0.2 sec. 55 mm ramp excitation.

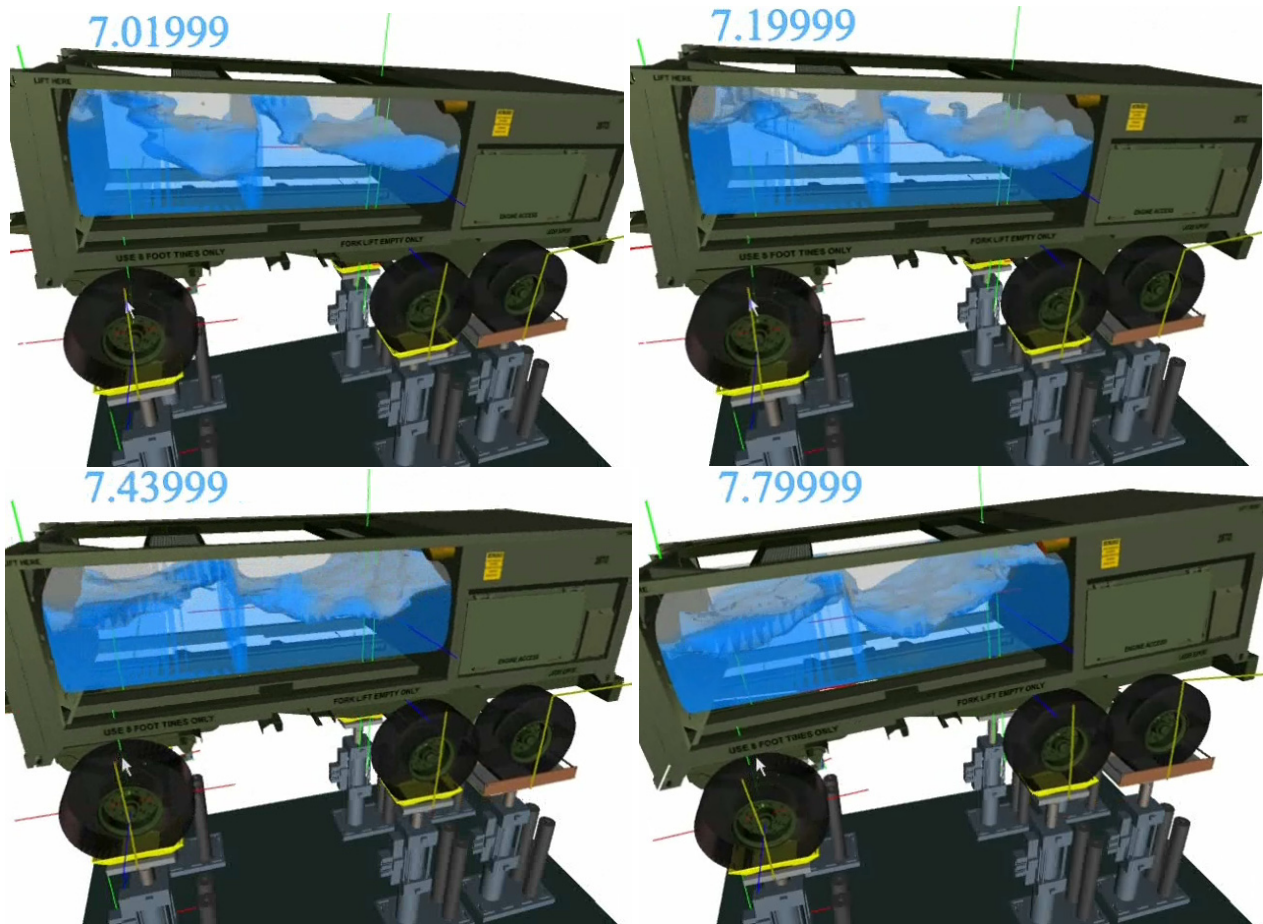


Figure 30 Snapshots of the trailer and liquid sloshing for the pitch 0.7 Hz, 140 mm harmonic excitation experiment.

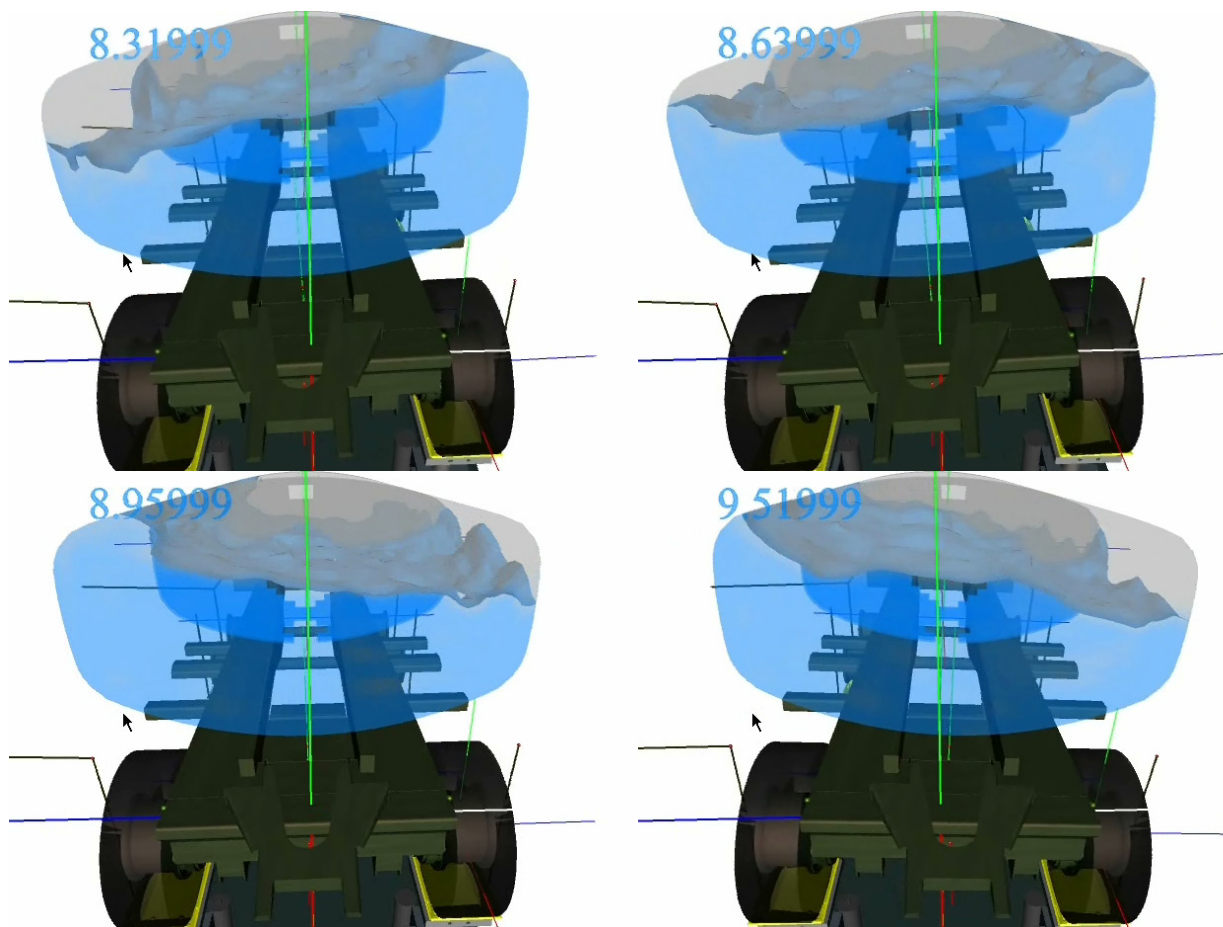


Figure 31 Snapshots of the trailer and liquid sloshing for the roll 0.5 Hz, 48 mm harmonic excitation experiment.

- The tank module (Hippo) was not securely mounted on the trailer. There was a clearance in the connection between the Hippo and the trailer, which based on visual observation and the sound produced is probably ± 20 mm. This means that the Hippo was in frictional contact with the trailer. For the low frequency runs the friction was enough to lock the tank on the trailer. But for the higher frequency runs and for the ramp runs the Hippo was sliding on the trailer. In the simulation model, it was assumed that the connection between the Hippo and the trailer was rigid.
- Tire damping as a function of tire deflection was estimated. However, this damping may be non-linear.
- Clearances in the trailer joints were not modeled since they were not measured.
- Non-linear behavior of the suspension leaf-springs. Friction and damping were estimated and added to the leaf-springs using truss elements. It is very hard to accurately characterize the non-linear stiffness, damping and friction of the leaf-springs.
- The security harness on the tank module on top of the PLS trailer contributed to the difference between the simulation and experiments especially for the higher frequency excitations.

Figures 30 and 31 show snapshots of the simulation of the trailer motion and liquid sloshing in the tank for two typical experiments.

6. CONCLUDING REMARKS

A finite element model for predicting the fully coupled dynamic response of flexible multibody systems and liquid sloshing for tanker trucks was presented. The model has the following characteristics:

- Parallel explicit time-integration solver.
- Library of accurate large rotation finite elements including: truss, beam, shell and solid elements. The elements only use Cartesian coordinates as DOFs.
- The fluid mesh is modeled using a very light and compliant solid mesh which allows the fluid mesh to move/deform along with the tank using the Arbitrary Lagrangian-Eulerian formulation.
- Acceptor-donor VOF algorithm for modeling the fluid's free-surface.
- The motion of the solid and fluid is referred to a global inertial Cartesian reference frame.
- A total Lagrangian deformation description is used for the solid elements.
- The penalty technique is used to model the joints.
- 1-Node tire model.

A validation study of the finite element model was carried out using a tanker-trailer mounted on an n-post

motion simulator. The study shows that the model can predict reasonably well, within 15-20% difference on average, the response of the trailer. There was no significant difference in error magnitude between the simulation and experiment for the empty tank and 65% filled tank runs. This shows that the difference between the simulation and experiment is not due to the fluid-structure interaction modeling and is mostly due to the trailer multibody model error sources identified in Section 5.

ACKNOWLEDGEMENTS

Support for this work provided by the US Army RDECOM-TARDEC, Warren, MI under SBIR grant number W56HZV05C0631 is gratefully acknowledged.

REFERENCES

1. *Hazardous Materials Risk Assessment*, U.S. Department of Transportation, Federal Motor Carrier Safety Administration, Publication No. FMCSA-RT-02-090, July 2002.
2. *Special analysis based on NFPA's Fire Incident Data Organization (FIDO)*. Quincy, MA: National Fire Protection Association, Fire Analysis and Research Division, 2000.
3. Wasfy, T.M., O'Kins, J. and Smith, S., "Experimental Validation of a Time-Accurate Finite Element Model for Coupled Multibody Dynamics and Liquid Sloshing," Paper No. 2007-01-0139, SAE 2007 Congress, Detroit, MI, April 2007
4. Gerrits, J. and Veldman, A., "Numerical simulation of coupled liquid-solid dynamics," *European Congress on Computation Methods in Applied Science and Engineering*, ECCOMAS 200, Barcelona, 2000.
5. Fekken, G., "Numerical simulation of a free-surface flow with moving rigid bodies," *Ph.D. Dissertation*, University of Groningen, 2004.
6. Rumold, W., "Modeling and simulation of vehicles carrying liquid cargo", *Multibody System Dynamics*, Vol 5, pp. 351-374, 2001.
7. Hirt, C.R. and Nichols, B.D., "Volume of fluid (VOF) method for the dynamics of free boundaries," *Journal of Computational Physics*, Vol. 39, pp. 201-225, 1981.
8. Youngs, D.L., "An interface tracking method for a 3D Eulerian hydrodynamics code," *Technical Report AWRE/44/92/35*, Atomic Weapons Research Establishment, 1987.
9. Souli, M. and Aquelet, N., "A new ALE formulation for sloshing analysis," *Structural Engineering and Mechanics*, Vol. 16(4), pp. 1-18, 2003.
10. Walhorn, E., Kolke, A., Hubner, B., and Dinkler, D., "Fluid-structure coupling within a monolithic model involving free surface flows," *Computers and Structures*, Vol. 83, pp. 2100-2111, 2005.
11. Tezduyar, T.E., "Finite element methods for flow problems with moving boundaries and interfaces,"

- Archives of Computational Methods in Engineering*, Vol. 8(2), pp. 8-130, 2001.
12. Nomura, T., "ALE finite element computations of fluid-structure interaction problems," *Computer Methods in Applied Mechanics and Engineering*, Vol. 112(1-4), pp. 291-308, 1994.
 13. Souli, M. and Zolesio, J.P., "Arbitrary Lagrangian-Eulerian and free surface methods in fluid mechanics," *Computer Methods in Applied Mechanics and Engineering*, Vol. 191, pp. 451-466, 2001.
 14. Braess, H. and Wriggers, P., "Arbitrary Lagrangian Eulerian finite element analysis of free surface flows," *Computer Methods in Applied Mechanics and Engineering*, Vol. 190, pp. 95-109, 2000.
 15. Stein, K. and Tezduyar, T., "Advanced mesh update techniques for problems involving large displacements," *Fifth world congress on computation mechanics*, WCCM V, Vienna, Austria, 2002.
 16. Battaglia, L., D'Elia, J., Storti, M., and Nigro, N., "Parallel implementation of free surface flows," *Mecanica Computacional*, Vol. XXIII, pp. 3119-3132, 2004.
 17. Idelsohn, S.R., Onate, E., Del Pin, F. and Calvo, N., "Fluid-structure interaction using the particle finite element method," *Computer Methods in Applied Mechanics and Engineering*, Vol. 195(17-18), pp. 2100-2123, March 2006.
 18. Bilarbegian, M. and Zu, J.W., "Dynamic analysis and simulation of vehicles carrying liquids during braking," ASME DETC2005-85102, 5th International Conference on Multibody Systems, Nonlinear Dynamics, and Control, ASME DETC, Long Beach, CA, 2005.
 19. Wasfy, T.M. and Noor, A.K., "Computational Strategies for Flexible Multibody Systems," *Applied Mechanics Reviews*, 56(6), 553-613, 2003.
 20. Wasfy, T.M. and Noor, A.K., "Modeling and sensitivity analysis of multibody systems using new solid, shell and beam elements," *Computer Methods in Applied Mechanics and Engineering*, Vol. 138(1-4) (25th Anniversary Issue), pp. 187-211, 1996.
 21. Wasfy, T.M., "A torsional spring-like beam element for the dynamic analysis of flexible multibody systems," *International Journal for Numerical Methods in Engineering*, Vol. 39(7), pp. 1079-1096, 1996.
 22. Wasfy, T.M., "Edge projected planar rectangular element for modeling flexible multibody systems," 19th Biennial Conference on Mechanical Vibration and Noise, Paper No. DETC2003-48351, 19th Biennial Conference on Mechanical Vibration and Noise, ASME International 2003 DETC, Chicago, IL, 2003.
 23. Wasfy, T.M., "Lumped-parameters brick element for modeling shell flexible multibody systems," 18th Biennial Conference on Mechanical Vibration and Noise, ASME International 2001 DETC, Pittsburgh, PA, 2001.
 24. Wasfy, T.M., "Modeling spatial rigid multibody systems using an explicit-time integration finite element solver and a penalty formulation," ASME Paper No. DETC2004-57352, 28th Biennial Mechanisms and Robotics Conference, DETC, Salt Lake, Utah 2004.
 25. Wasfy, T.M., "Asperity spring friction model with application to belt-drives," Paper No. DETC2003-48343, Proceeding of the DETC: 19th Biennial Conference on Mechanical Vibration and Noise, Chicago, IL, 2003.
 26. Leamy, M.J. and Wasfy, T.M., "Transient and steady-state dynamic finite element modeling of belt-drives," ASME Journal of Dynamics Systems, Measurement, and Control, Vol. 124(4), pp. 575-581, 2002.
 27. Wasfy, T.M. and Leamy, M.J., "Modeling the dynamic frictional contact of tires using an explicit finite element code," ASME DETC2005-84694, 5th International Conference on Multibody Systems, Nonlinear Dynamics, and Control, ASME DETC, Long Beach, CA, 2005.
 28. Wasfy, T.M. and Leamy, M.J., "Dynamic modeling of synchronous belt-drives using an explicit finite element code," ASME DETC2005-85103, 5th International Conference on Multibody Systems, Nonlinear Dynamics, and Control, ASME DETC, Long Beach, CA, 2005.
 29. Meckstroth, R.J., Wasfy, T.M., and Leamy, M.J., "Finite element study of the dynamic response of serpentine belt-drives with isolator clutches," SAE 2004 Congress, Paper No. 2004-01-1347, Detroit, MI, 2004.
 30. Chorin, A.J., "A Numerical Method for Solving Incompressible Viscous Flow Problems," *Journal of Computational Physics*, Vol. 2(1), 1967.
 31. Wasfy, T.M., West, A.C. and Modi, V., "Parallel finite element computations of unsteady incompressible flows," *International Journal for Numerical Methods in Fluids*, Vol. 26(1), pp. 17-37, 1998.
 32. DIS (Dynamic Interactions Simulator), <http://www.ascience.com/ScProducts.htm>, Advanced Science and Automation Corp., 2007.

APPENDIX: EXPLICIT SOLUTION PROCEDURE

The solution fields for modeling the solid, fluid and liquid free-surface are defined at the model nodes. These are:

- Solid translational positions.
- Solid translational velocities.
- Solid translational accelerations.
- Solid rotation matrices.
- Solid rotational (angular) velocities.
- Solid rotational (angular) accelerations.
- Fluid velocities.
- Fluid accelerations.
- Fluid pressure.
- Fluid pressure rate.
- Volume-of-fluid.

- Eddy kinetic energy
- Eddy kinetic energy rate.

The explicit time integration solution procedure for modeling the coupled response of the solid (multibody system), fluid, and liquid free-surface (using the VOF formulation) predicts the time evolution of the above response quantities. The procedure is implemented in the DIS [32] (Dynamic Interactions Simulator) commercial software code and is outlined below:

- 1) Prepare the run:
 - a. Set the initial conditions for the solution fields identified above.
 - b. Create a list of all the finite elements (including both solid and fluid elements).
 - c. Create a list of elements that will run on each processor. This is done using an algorithm which tries to make the computational cost on each processor equal.
 - d. Create a list of all the constraints (including both solid and fluid constraints).
 - e. Calculate the solid masses for each finite element node by looping through the list of finite elements. Note that the solid masses are fixed in time.
 - f. For each node create a list of corner and edge nodes that are connected to it using fluid volume elements.
 - g. VOF preparations:
 - i. Find a list of the volume fluid elements.
 - ii. Create a list of fluid volume elements that will run on each processor. This is done using an algorithm which tries to make the computational cost on each processor equal.
 - iii. For each element find all neighboring elements.
 - iv. For each element find the element VOF using the nodal VOF.
 - v. Re-interpolate the elements' VOF to nodal VOF.
 - h. Loop over all the elements and find the minimum time step for the explicit solution procedure.
 - i. Loop over all the elements and create a list of wall nodes. For each wall node find the list of fluid boundary elements.
- 2) Loop over the solution time and increment the time by Δt each step while doing the following:
 - a. Set the nodal values at the last time step to be equal to the current nodal values for all solution fields.
 - b. Do 2 iterations (a predictor iteration and a corrector iteration) of the following:
 - i. Initialize the nodal fluxes to zero. Those include: solid forces, solid moments, fluid forces, boundary fluid forces, and pressure fluxes. In addition, the lumped nodal fluid volume and fluid mass vectors are also initialized to zero.
 - ii. Calculate the nodal solid and fluid fluxes and the lumped fluid volume/mass vectors by looping through all the elements while calculating and assembling the element nodal fluxes and vectors. This is the most computationally intensive step. This step is done in parallel by

- running each list of elements identified in step 1.c on one processor.
- iii. Find the nodal values at the current time step using the semi-discrete equations of motion and the trapezoidal time integration rule (Equations 1-5 and 19-21).
- iv. Execute the solid and fluid constraints. The constraints prescribe the nodal values.
- v. Apply fluid-structure interface boundary conditions for all wall nodes found in Step 1.i (see Equations 22, 23). This is done by doing the following for each wall node:
 1. Find the normal to the surface at the wall node.
 2. Normalize the surface normal.
 3. Find the solid, fluid bulk and fluid boundary forces in the directions normal and tangent to the surface.
 4. Find the normal and tangential solid and fluid accelerations using the trapezoidal integration rule and the wall slip percentage.
- vi. Set the pressure boundary conditions at the free surface.
- vii. Update the VOF field:
 1. For each fluid element calculate the element volume. This step is done in parallel using the list of fluid elements for each processor found in Step 1.g.ii.
 2. For each fluid element find the apertures through which the fluid convects to each neighboring element. This step is done in parallel using the list of fluid elements for each processor found in Step 1.g.ii.
 3. For each fluid element use the apertures, the element volume, the element current VOF value, and the element nodal velocities to update the VOF value of all neighboring elements by finding the volume of fluid that left the element during that time step using Equations 30-35. This step is done in parallel using the list of fluid elements for each processor found in Step 1.g.ii. Note that this step depends on the order of the elements in the list of elements. However, since the updates of the VOF field between solution time steps are small, therefore this dependence is generally very small. In order to assure minimum dependence on the elements' order, at a time step the elements are updated from first to last, then at the next time step they are updated from last to first.
- viii. Average the fluid pressure (This step eliminates the pressure checker-boarding effect and allows use of equal order interpolation for both pressure and velocity).
- ix. Go to the beginning of step 2.

An advantage of explicit solution procedures is that they are "embarrassingly" parallel. The above procedure achieves near linear speed-up with the number of processors.